Mid-Infrared Studies of Cold Dust Distribution in Bipolar Planetary Nebulae

(   )

26   12   (   )

Abstract

Mass loss process in the final evolutional stage of low mass stars is quite important to understand not only the cycle of matters in the Universe but also their stellar evolution. Classically it is believed that the circumstellar matter expand isotopically and form spherical symmetric shells. However bipolar planetary nebulae cannot be explained by the classical, isotropic mass loss. One possible explanation proposed is that a pair of expanding bubbles is made by the interaction between fast wind and a dense circumstellar torus in the equatorial plane (GISW model). The GISW model naturally explains the origin of the bipolar lobes, but it does not address the origin of the equatorial disk or torus at all.

To investigate the equatorial disk or torus in detail, longer wavelength mid-infrared observations with sufficient spatial resolution are absolutely essential. We have carried out mid-infrared observations of three bipolar planetary nebulae, NGC6302, Mz3, Hb5. These are very famous planetary nebulae and very bright objects at the mid-infrared wavelengths.

A new mid-infrared camera MAX38 developed by ourselves has been used for this study. It was attached on the miniTAO 1.0 meter telescope at the summit of Co.Chajnantor, which is the highest astronomical site on the globe. Thanks to the high altitude of 5,640m and dry weather condition, we can access the 30 μm wavelength range from the ground.

Mid-infrared images of the planetary nebulae at 18, 25, 31, and 37 μm have been successfully obtained. These are the first spatially resolved images of the planetary nebulae at the wavelengths longer than 30 μm. The images of NGC6302 show an extended structure, and the detailed characteristics of the structure varies with the wavelengths. The peak is located at eastside of the center at 18.7 μm, at almost center at 31.7 μm, and at western-south side at 37.2 μm. This may be explained by the extinction effect of the dense dusty torus. The mid-infrared images of Mz3 show three components, a central bright core and filamentary extended structure in the north and the south. This structure is quite similar to the bipolar planetary nebulae seen in the visible image. These are the first images of Hb5 at the mid-infrared wavelengths range with a spatial resolution higher than 8 arcsec. On the contrary, the images of Hb5 at shorter than 25 μm seem very compact and

i

not extend .

It is a surprising result that an unexpected bright 30 μm source are detected at the center of the three nebulae. It suggests a presence of a cold dust component close to the central star. The mass of the cold dust component is estimated with a simple model. The estimated dust masses of the cold component of NGC6302, Mz3, and Hb5 are 2.5×10^{-2}, 2.2×10^{-3}, and $1.0 \times 10^{-3} M_\odot$, respectively.

These are up to 100 times larger than the dust mass estimated in previous studies. The morphological structure of the cold dust component are estimated based on the ratio of the luminosity of the central star and the cold dust. It suggests that there are geometrical thick tori with opening angles of 50, 20, and 26 degree for NGC6302, Mz3, and Hb5 on the equatorial plane, respectively.

In addition, the tori seem to be very compact in the 30 μm images. This may be interpreted with two possibilities. One is the optical thickness. In this case, inner warm region which mainly absorbs the stellar radiation should be completely obscured by the outer cold torus, because there are no warm components in the spectral energy distribution. This requires the outer torus to be optically thick at the shorter side of the mid-infrared wavelengths. Furthermore the inner region needs to have almost the same opening angle as the outer torus. The other possibility is dust grain growth in the torus. Since larger dust grains have relatively low emissivity, the thermally balanced temperature is lower than the smaller dust if they receive the same input radiation.

These results give the constraints on the structure of the dusty torus and provide important information to understand the strong mass loss on the equatorial plane.

Contents

List of Figures

List of Tables

Chapter 1

Introduction

Planetary Nebulae (PNe), named by William Herschel are the most beautiful objects in the night sky. Various shapes and vivid colors of them fascinate many people including astronomers. Actually a photo of NGC6302 taken by Hubble Space Telescope (HST) is one of the most popular astronomical images in the world (Fig 1.1). It has a slender waist and flared lobes and looks like a butterfly. This kind of the object is called as a bipolar PN. The bipolar PNe are not only attractive but also interesting objects for the modern astronomy. There are two important open questions. One is about the supply of the dust in galaxies, and the other is about the formation mechanism of the bipolar structure.

1.1 Dust Budget Problem in the Universe

Details of formation and growth processes of dust in the Universe remain as an open question. Two major suppliers of the dust are under discussion; evolved stars with massive progenitors, and ones with low and intermediate progenitors. Extensive observations have been carried out so far, but they have not reached a clear answer to the question. Theoretical studies have predicted that the super novae (SNe) supply a huge amount of the dust, typically 10^{-1} M$_\odot$ per object. This is consistent with the fact that strong dust emissions have been detected in many galaxies in the early Universe (Bertoldi et al. 2003; Priddey et al. 2003). Although observations have only found much lower amount of dust in many of nearby SNe, the latest observations by ALMA and Herschel (Matsuura et al. 2011; Indebetouw et al. 2014) have revealed that there are enough amount of dust in SN1987A.

Low and intermediate mass ($0.8 - 8$ M$_\odot$) stars are the other important candidate of the dust suppliers because they dominate the stellar population in our Galaxy. Their dust formation mainly occurs in their evolutional stage in Asymptotic Giant Branch Star (AGB) phase, and its details are thought to strongly depend
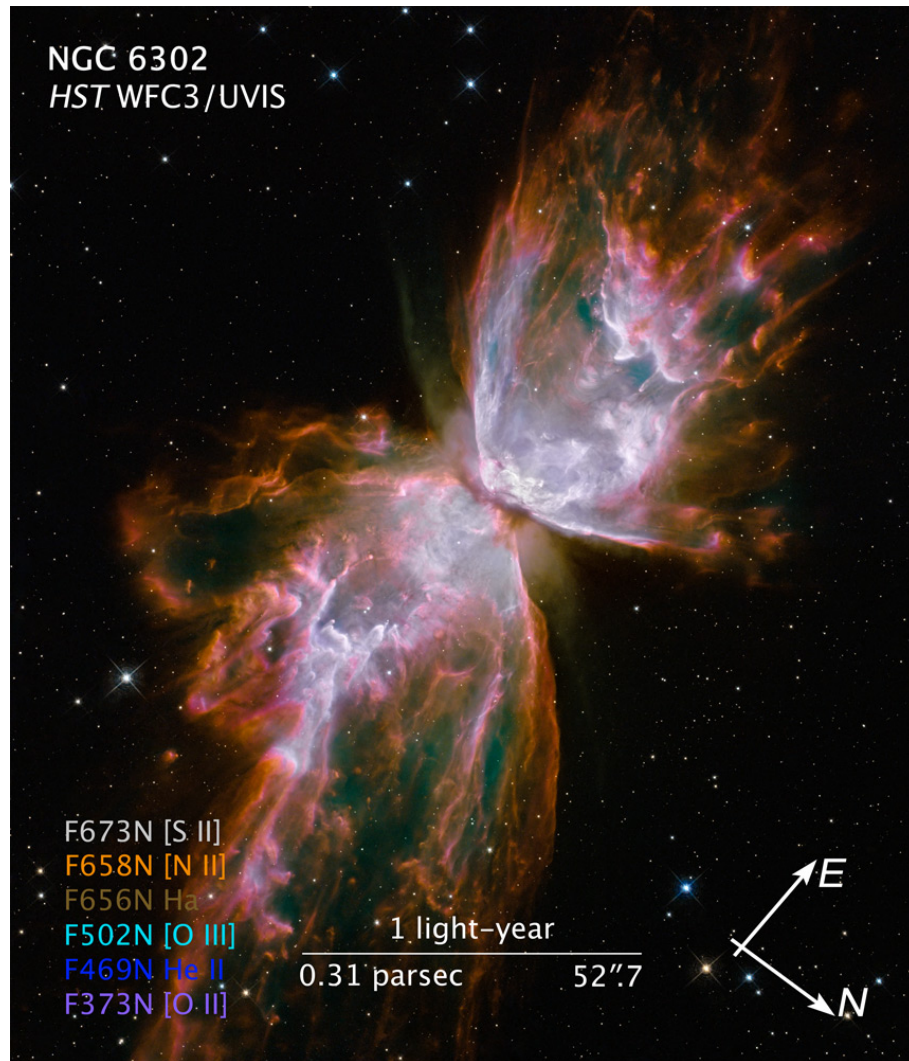
Figure 1.1: An optical image of NGC6302 obtained by Hubble Space Telescope.

on their progenitor masses. Around low mass AGB stars whose progenitor masses are $0.8 - 3$ $M_\odot$ isotopic dust/gas shells have been observed. One impressive example is the circular shell around an AGB star U Hyr observed at 90 μm by AKARI (Izumiura et al. 2011). In addition geometrically thin log-lived disks are found in some PPNe.

Intermediate mass stars are also, or more important dust supplier than low-mass stars since their mass loss per star is expected to be heavier than that of the lower mass stars. However they have not been extensively investigated so far. They are relatively rare objects in our galaxy since they evolve from AGB to PPNe phase very fast. Typical duration is only from $100 - 10,000$ years (e.g. Sabbadin 1986; Dopita et al. 1987; Vassiliadis & Wood 1994). In addition observations at visible wavelengths are very difficult due to their heavy obscuration. Because of large mass of their progenitor, they commonly surrounded with high amount of dust, which cause heavy obscuration in visible wavelength. Therefore number of the visible objects known as the AGB stars or the PPNe evolved from the intermediate stars is quite limited, though efforts to find out this kind of stars have been extensively continued (Ramos-Larios et al. 2009, 2012).

To shed light on the difficulty, bipolar PNe should be focused. Bipolar PNe are considered to evolve from the intermediate stars since their distribution in the sky is strongly concentrated on the Galactic plane (Corradi & Schwarz 1995; Manchado et al. 2000; Stanghellini et al. 2002). Figure 1.2 displays the galactic distributions of round, elliptical, and bipolar PNe reported by Manchado et al. (2000). The scale height <z> of bipolar PNe is smaller than the other PNe, indicating that their progenitor is relatively massive. In the main sequence phase of the intermediate mass stars, the convection envelope is thought to reach high temperature such as $\sim 5 \times 10^7$K, and it initiates H-burning within the convective envelope (hot bottom burning). This process effectively converts ^{12}C into ^{14}N, therefore the abundance of N is expected to be relatively higher. This is consistent with the observational fact that <N/H> value of the bipolar PNe is systematically higher than that of the other PNe (e.g. Corradi & Schwarz 1995; Manchado et al. 2000; Stanghellini et al. 2002).

The bipolar PNe are quite useful objects to study the mass loss history of the intermediate mass stars. Especially spatially resolved observations are important since the spatial distribution of the dust records the history of the mass loss and the dust formation. This may give a key to understand the evolution of the intermediate mass stars, and solve the longtime mystery of the dust budget in the Universe.
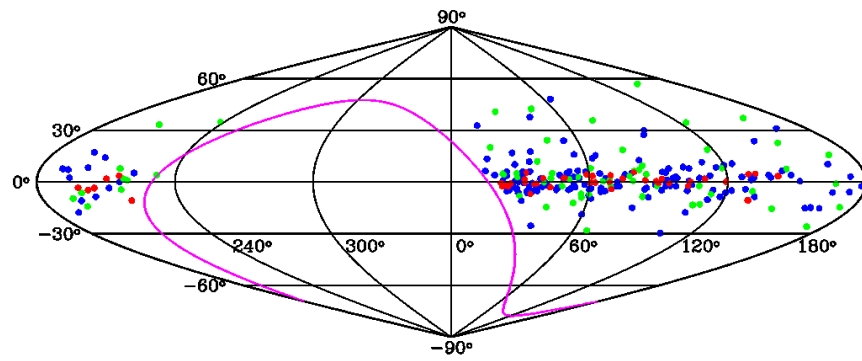
Figure 1.2: Bipolar PNe distribution in our Galaxy . Red dots is bipolar, bule dots is elliptical, and green dots is round PNe (Manchado et al. 2000).

1.2 Shaping Problem of the Bipolar Nebulae

The other problem of the bipolar PNe is how to form their asymmetric shape. The mass loss in the AGB phase is normally believed to be spherically isotopic and form spherical symmetric shells. Such round shape shells are observed in many AGB stars (Mauron & Huggins 1999; Izumiura et al. 2011; Maercker et al. 2012). Its expanding velocity is typically 10 km s^{-1}. On the contrary mass loss with high expanding velocity of up to 10^3 km s^{-1} are detected in some post-AGB stars and Planetary Nebulae (PNe). Kwok et al. (1978) suggested that this fast stellar wind arises in the PNe phase after slowly expanding and dense ejection in the AGB phase. This is called the interacting stellar wind (ISW) model.

However these classical and isotropic mass loss cannot explain the asymmetric structures seen in the bipolar PNe. One possible explanation proposed by Calvet & Peimbert (1983) is that pair expanding bubbles is made by the interaction between fast wind and a dense circumstellar torus in the equatorial plane. This hypothesis is called Generalized ISW (GISW) model, and has been supported by numerical analysis (Kahn & West 1985; Icke 1988; Frank 1994) and some observations (Balick 1987). The GISW model naturally explains the origin of the bipolar lobes, but it does not address the origin of the equatorial disk or torus at all. Some mechanism of the mass loss in the equatorial plane is expected. Two major models have been proposed to explain the equatorial mass loss so far. One is a magnetic field with AGB stars, and the other is a binary interaction.

(i) Magnetic field with AGB stars

It is expected that a dynamo between a surface of rapidly rotating AGB star and a slowly rotating envelope produces a magnetic field. Chevalier & Luo (1994), Blackman et al. (2001) pointed out that a toroidal magnetic field can increase in the shocked bubble formed in mass loss process and dominate the gas thermal pressure. Such a toroidal magnetic field possibly suppresses mass loss in the equatorial plane and causes an asymmetric shape of bipolar PNe, if the magnetic field can evolve strong enough. This model requires the strong magnetic field of larger than 10^3 Gauss. Practically strong magnetic fields between 10^3 to 10^9 Gauss have been found in 10 – 30% of all white dwarfs (Leone et al. 2014). However such a strong magnetic field has not been discovered in the PNe so far. Previously Jordan et al. (2005) reported the strong magnetic field in two PNe, but this was rejected by the follow-up observations (Leone et al. 2011; Bagnulo et al. 2012; Jordan et al. 2012; Tocknell et al. 2014). Currently there seems no observational evidence of the strong magnetic field in PNe.

(ii) Binary interaction

A closed binary system creates a common envelope around them and it may case the asymmetric shape of PNe. When the primary evolves up the red giant branch and its radius reaches its tidal radius, the matter from the primary will be ejected on the equatorial plane by the secondary (Morris 1981; Soker 1998; Soker & Rappaport 2000) calculated the interaction between a slow AGB wind and collimated fast wind blowing in a main-sequence or white dwarf phase, and found that the collimated fast winds compress AGB slow winds to create the dense disk on the equatorial plane. However it is not clear whatever all of bipolar PNe are binary or not.

Unfortunately both of those hypotheses cannot completely explain the cause of the mass loss on the equatorial plane. Further studies, especially observational studies of the equatorial structure, are eagerly needed.

To investigate the dust in the bipolar PNe, access the dust budget problem, and the shaping problem, longer mid-infrared observations with sufficient spatial resolution are absolutely essential. The central region is quite dense and sometimes optically thick even in the 10 μm wavelength region. In addition the temperature of the dust is considered to be around 100 K according to the infrared spectra obtained by ISO and Spitzer. These indicate that observations at 20 or longer wavelengths are needed to observe the dense central region. Furthermore sufficiently high spatial resolution of at least 10 arcsecond is required to resolve the central region and the lobes even for the nearest PNe. Such kinds of observations used to be very difficult, but our development of a new telescope at the world highest site and a new camera which can observe 30 μm wavelength range enable us to carry out such observations.

1.3   Scope of This Thesis

In this paper we report the observational results of three bipolar PNe at 18–37 μm wavelength range and discuss the dust distribution in the nebula. In section 2 we describe the telescope and the instrument which we have developed and used for this study. In section 3 details of observations are described. In section 4 results of the observations are presented, and in section 5 the structure of the central dusty tori will be discussed.

Chapter 2

miniTAO/MAX38

2.1 miniTAO

Mini TAO is a pathfinder telescope of Tokyo Atacama Observatory (TAO) project (Yoshii et al. 2002, 2014). It is located at the top of Cerro (Co.) Chajnantor in the Atacama Desert, northern Chile. The plateau of the Atacama Desert is at an altitude over 5,000 m and Co.Chajnantor is at an altitude of 5,640 m. Thanks to this extremely high altitude, Co.Chajnantor is one of the best sites for infrared and radio astronomy. In fact, several radio observatories including Atacama Submillimeter Telescope Experiment (ASTE) , NANTEN-2, Atacama Pathfinder Experiment (APEX), Cosmic Background Imager (CBI), and Atacama Large Millimeter/Submillimeter Array (ALMA) have been constructed.

The precipitable water vapor (PWV) is 0.4 to 1.3 mm at miniTAO site. It is much lower than that at the Mauna Kea Observatory of 0.9 to 2.8 mm in yearly average (see Sako et al. 2008). Figure 2.1 shows the atmospheric transmission at Co. Chajnantor and Mauna Kea calculated with an ATRAN model (Lord 1992). Due to the extremely low PWV, we can carry out observations in the $30\,\mu$m wavelength region, which has never been observed from any other ground-based telescopes. It has been demonstrated by practical observations (Miyata et al. 2012) that the atmospheric windows around $30\,\mu$m are transparent enough for the astronomical observations.

Figure 2.2 displays a photo of the miniTAO telescope and our developed mid-infrared camera MAX38. The telescope optics is a standard Ritchey-Chretien type reflector with an aperture of 1,042 mm and optimized for infrared observations. The telescope was installed in the summit on March 2009. More details of the telescope can be seen in Sako et al. (2008).
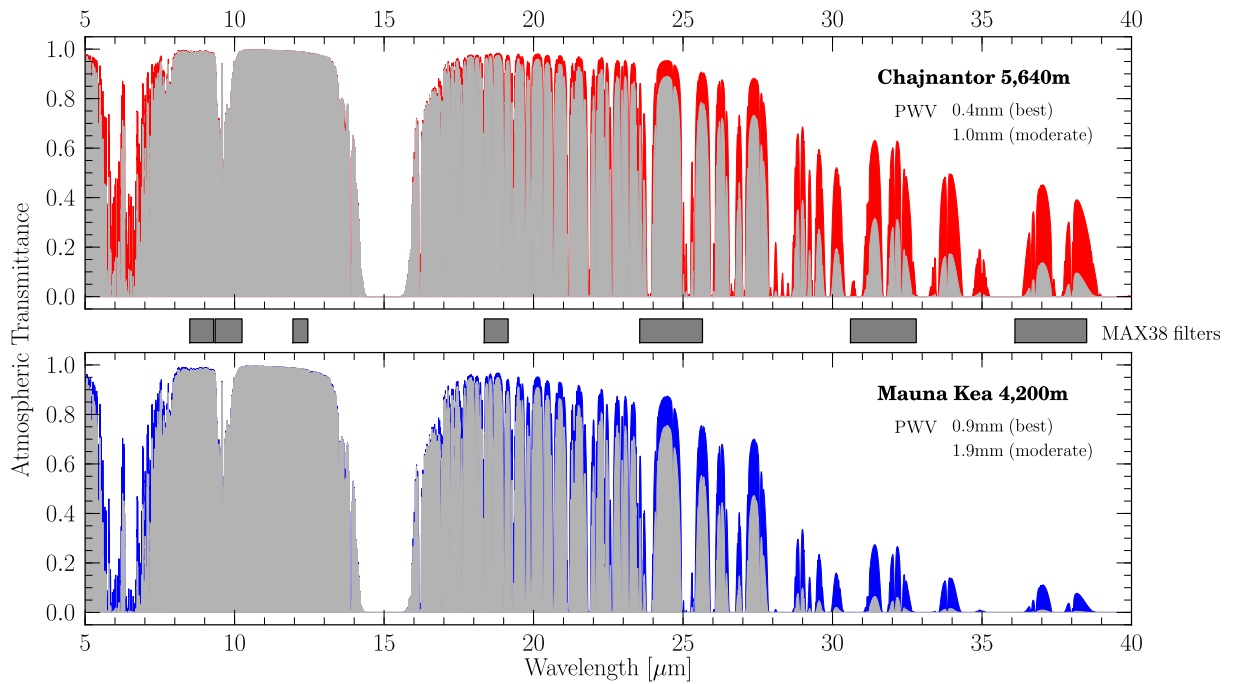
Figure 2.1: Transmittances at CHAJNANTOR and MAUNAKEA calculated with best and moderate PWV (Asano et al. 2012)

2.2 MAX38

Mid-infrared Astronomical eXprorer (MAX38) is our newly developed instrument for the miniTAO telescope (Miyata et al. 2008). Table 2.1 summarizes the specification of MAX38. The filter list and the measured sensitivity and Point Spread Function (PSF) of MAX38 are shown in Table 2.2 and Figure 2.3.

One of the most important advantages is high spatial resolution at long mid-infrared wavelengths range. The spatial resolution of 4.9, 7.6, and 8.5 arcsecond has been achieved at 18.7, 31.7, 37.3 μm. These are almost equivalent to the diffraction limited spatial resolution. The sensitivities are estimated to be 2.2, 38, 70 Jy for 1σ1second at 18.7, 31.7, and 37.2 μm respectively. Those are enough for observing bright objects such as nearby planetary nebulae. More details of the on sky performance of MAX38 were extensively discussed in Asano et al. (2012).

Detector	Si:Sb BIB 128×128 array	DRS Technologies,Inc.
Pixel scale	1.26 arcseconds/pixel	
Field of View	161× 150 arcseconds	Imaging area
Wavelength	8 – 38 μm	

Table 2.1: miniTAO/MAX38 specifications
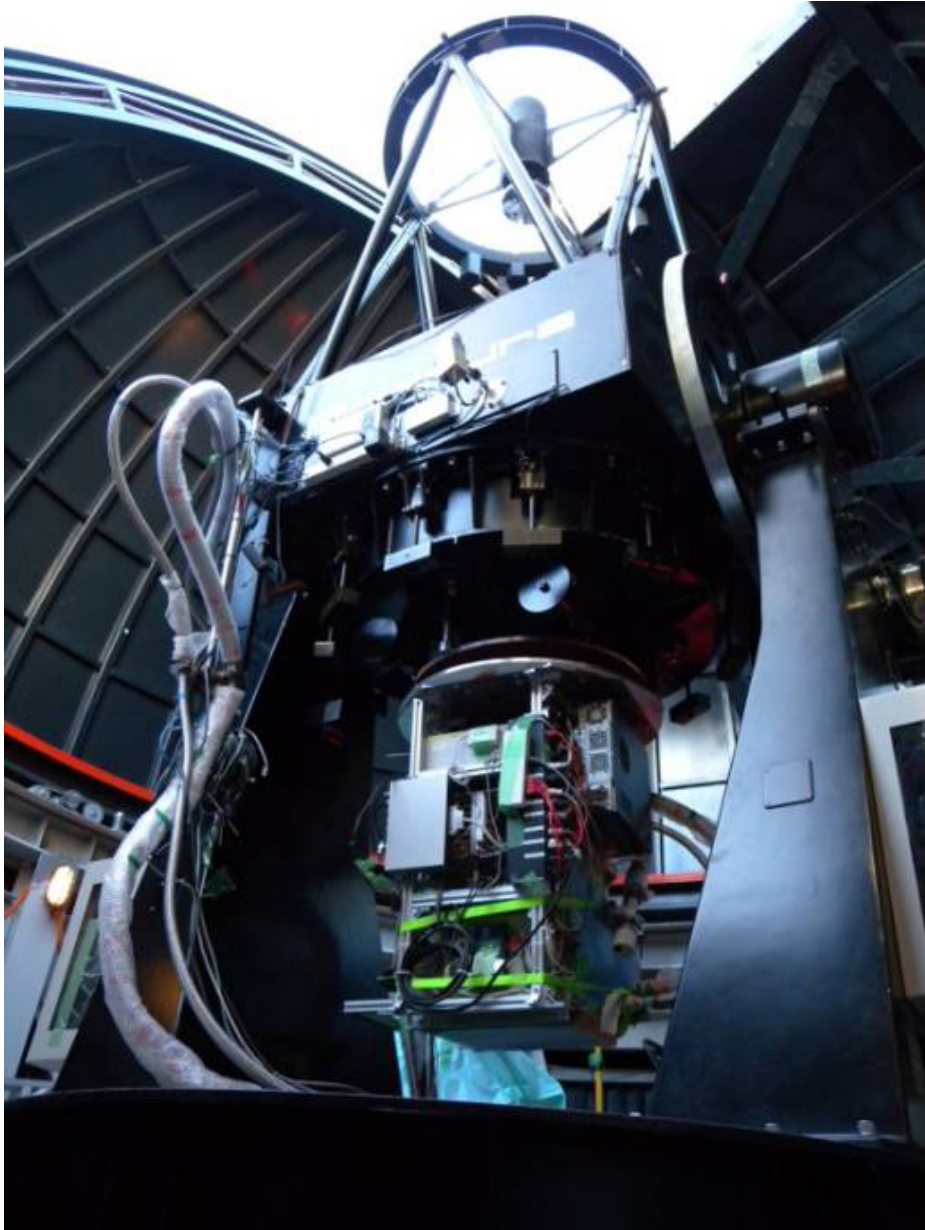
Figure 2.2: MAX38 attached with miniTAO 1.0 meter telescope. MAX38 on the Cassegrain focus of the telescope.

Name	Central wavelength [μm]	Band width [μm]	Measured FWHM [arcsec]	Diffraction limit [μm]	Atmosphere trans- mittance	Filter trans- mittance	Detector efficiency [%]	System efficiency [%]	Sensitivity [Jy/1σ1sec]
J089W08	8.9	0.8	2.39	2.19	0.90	0.8	6.9	3.37	1.7
J098W09	9.8	0.9	2.65	2.41	0.60	0.9	5.4	2.76	2.8
J122W05	12.2	0.5	3.15	3.00	0.75	0.8	12	5.27	3.1
R187W09	18.7	0.9	4.91	4.60	0.82	0.50	14	3.33	2.2
MMF31	31.7	2.2	7.56	7.79	0.33	0.4	64	14.7	38
MMF37	37.3	2.4	8.51	9.17	0.23	0.40	32	5.45	70

Table 2.2: On-sky performances of MAX38 including measured PSF, diffraction limit, system efficiency, and sensitivity for each filter

2.3   30 μm Observations from Ground

There are some difficulties in reduction and calibration of images at 30 μm taken by ground based telescopes; residual pattern in sky background, rapid fluctuation of atmospheric transmittance, and the lack of photometric standard stars. In this section we describe these difficulties and explain how to overcome them.

2.3.1   Residual Pattern in Sky Background

Since the thermal background from the sky and the telescope is huge and varies very fast in the mid-infrared wavelength region, the accurate subtraction of the background is critically important. Chop-and-nod technique is generally used for these observations and successfully achieves the accurate subtraction in the N- and the Q-band. However, the situation is more severe at the 30 μm. Because the background at 30 μm is more unstable, significant patterns in the subtracted images sometimes remain. These residuals degrade accuracy and feasibility of the images and make it difficult to detect the diffuse components in extended objects. To overcome this problem, we have developed a reduction method called weighted averaging method. This is the method of composing a sky frame by a linear combination of some sky images and subtracting it from an object frame to minimize the residual patterns. Further details are shown in doctral thesis of Nakamura (2012). We have applied this method to our images and demonstrated the effectiveness of this method for the reduction of relatively faint and extended objects.

2.3.2   Rapid Fluctuation of Atmospheric Transmittance

Another serious difficulty on the 30 μm observations is rapid fluctuation of atmospheric transmittance at the wavelengths. To eliminate the harmful effects of the unstable transmittance, we have applied the following techniques in the observation and the reduction procedures.

   1) Consecutive observations of a target and a standard star
Since the sky transmittance strongly vary with time, it is better to observe standard stars close to the target observations. In normal cases we have carried out the standard observations just before or after the target. It is helpful to minimize the difference of the observation conditions between the target and the standard stars. Airmass is another concern to cause the different sky conditions. We have chosen the standard stars at the same airmass as the target as far as possible.

   2) Calibration of the sky transmittance based on PWV measurements
Since atmospheric absorption around 30 μm is mainly carried by water in atmosphere, it is naturally expected to be correlated with the perceptible water vapor
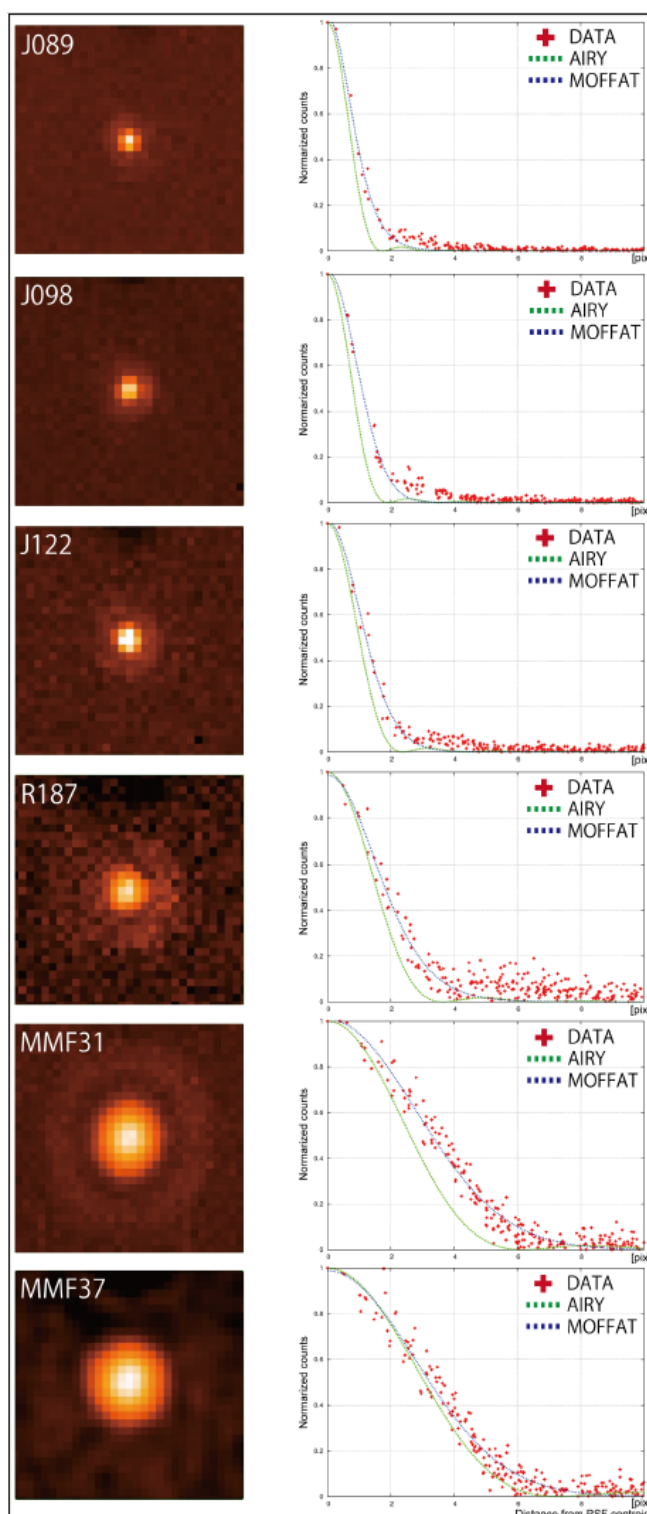
Figure 2.3: PSF images (left panels) and their radial profiles (right panels) of the MAX38 filters. Sizes of the PSF images are 38×38 arcsecond². In right panels, observed radial profiles are shown by crosses, while Moffat functions fitted to the data and shown by blue dotted lines. Additionally, we plot Airy functions calculated from optical design with green dotted line, see Asano et al. (2012)

(PWV). Fortunately PWV in the Chajnantor area is continuously monitored by a radio telescope project APEX (Atacama Pathfinder Experiment) located on the foot of the Chajnantor (its altitude is approximately 5,000m) every 10 minutes and the data is automatically opened for the public via their web page. Therefore the PWV value at the observations can be easily known, and used for the estimation of the sky transmittance. We employ the ATRAN model Lord (1992) for the estimation. Corrected value of the transmittance was typically lower than 5% when the sky condition was good.

Although this calibration is quite useful, it may include some worries as followings. Was the PWV of the line of sight of the observation completely the same as the monitored value by APEX, or was the PWV varied with the direction of the sky? Did the difference in the altitude between the APEX site (5,000m) and the miniTAO site (5,640m) cause a critical difference of the PWV? A method to cross-check the feasibility of the transmittance calibration is needed to dispel those worries.

Brightness of the sky background is expected to be a good indicator of the sky transmittance. Assuming that the atmosphere is simply a single layer and is in thermal equilibrium,

$$\epsilon_{atm} + \tau_{atm} = 1 \tag{2.1}$$

where ϵ_{atm} is the emissivity of atmosphere and τ_{atm} is the transmittance coefficient of atmosphere. This equation shows that τ_{atm} is equal to $1 - \epsilon_{atm}$. In other words, absorbed fraction can be indicated by sky background emission.

The clear correlation between the brightness of the background and the atmospheric transmittance has been detected in some data obtained by miniTAO/MAX38. Fig 2.3.2 is a practical example of this correlation. The vertical axis represents the measured count of a star, and the horizontal axis represents the background flux measured in the blank sky area. Linear correlation is clearly displayed, indicating that the brightness of the background can be used as the cross-checker of the sky transmittance.

In the practical procedure of the reduction, the background fluxes of the target frame and the standard frame were measured and compared with each other. If the difference were significantly large, these frames would be removed from the photometric data. However none of the frames were removed in this work fortunately because the sky condition was excellent during the observations.

2.3.3   Lack of Photometric Standard Stars

The other concern to achieve the accurate photometry is the lack of photometric standard stars in the 30 μm wavelength range. At shorter wavelengths normal
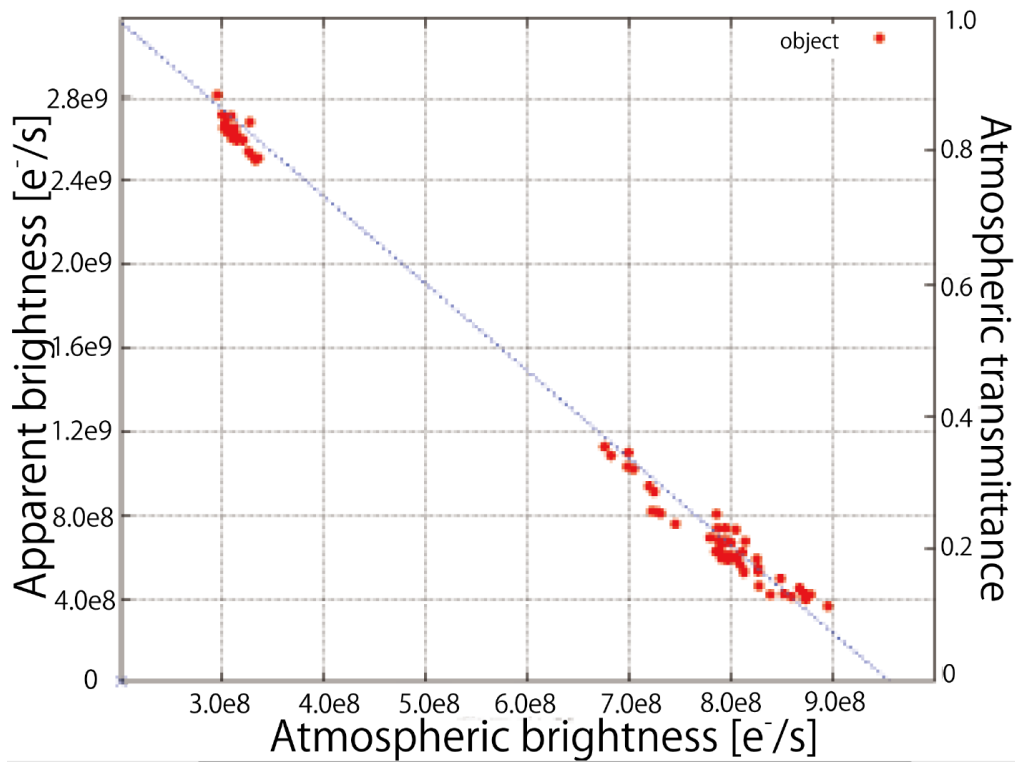
Figure 2.4: A relation between the atmospheric brightness and the apparent brightness of a star at 31.7 μm. Filled circles represents the observed data and a dotted line represents a fitted line derived from least square method. A clear correlation between apparent brightness and atmospheric brightness is displayed. Asano et al. (2012)

stars are commonly used as the photometric standards. For example the stars which was well examined and listed by Cohen et al. (1999) is used for the calibration of N- and Q-band data obtained ground-based mid-infrared cameras such as Subaru/COMICS. However these stars are too faint at the 30 μm. Typical flux of these stars is several Jy at 30 μm which is approximately one-fourth of the sensitivity of the MAX38 (Asano et al. 2012). Therefore these stars cannot be used for the 30 μm observations of MAX38. Some giant stars such as VX Sgr, W Aql, and α Boo, are much brighter at 30 μm. Typical flux of these stars at 30 μm is 500Jy or higher. Although these stars are known as variable stars at visible wavelength, Monnier et al. (1998) reported that the variation of late type super giants or giants at 8–13 μm were only at the order of ± 20% over several years. In addition the variability decrease at longer wavelengths (Lockwood & Wing 1971; Harvey et al. 1974; Le Bertre 1992, 1993; Little-Marenin et al. 1996; Smith et al. 2002).

Chapter 3

Observation

3.1 Target Selection

We observed three PNe of NGC6302, PN Mz3, and PN Hb3 in this study. These PNe meet the following two criteria. (1) The mid-infrared flux is bright enough for MAX38, specifically brighter than 70 Jy at $30\,\mu$m. When the flux at $30\,\mu$m has not directly measured, it was estimated by linear-interpolation of the IRAS $25\,\mu$m and $60\,\mu$m fluxes. (2) the declination is less than 30 degree to be accessible from the southern hemisphere. These PNe are very famous objects and listed in the many catalogues of PNe such as Acker et al. (1992), Robertson-Tessi & Garnett (2005) and so on. Basic parameters of the targets are described in Table 3.1.

Our targets are ones of the brightest PNe in the mid-infrared wavelengths, and these would be intrinsically luminous objects, i.e., relatively massive objects. This could cause the selection bias on our discussion if this were the case.

Figure 3.1 shows the relation between the fluxes at $60\,\mu$m and the distances of PNe listed in Corradi & Schwarz (1995). The fluxes at $60\,\mu$m were obtained by IRAS and they can be considered as cold dust emission. A strong correlation is clearly seen, and our samples are plotted on the nearest side of the distribution. This indicates that the brightness of our sample is due to their near distance rather than to their massive progenitor. We think that our samples are less biased in their progenitor mass.

3.1.1 PSFs and Photometric standard stars

Accurate measurement of the point spread functions (PSFs) is essentially important for our study. Four bright stars (VX Sgr, W Aql, V1185 Sco, and Alf Boo) were observed as the PSF reference stars. Alf Boo is a famous red giant and is a perfect point-source even in the mid infrared wavelengths. VX Sgr is a red su-

Table 3.1: Target list

Object Name	RA (J2000)	Dec (J2000)	IRAS 25μm Flux[Jy]	Expected 30μm Flux [Jy]	IRAS 60μm Flux[Jy]
NGC6302	17 13 44.211	-37 06 15.94	335.9	410	849.7
Mz3	16 17 13.40	-51 59 10.6	343.4	334	277.0
Hb5	17 47 56.187	-29 59 41.91	79.2	87	134.5
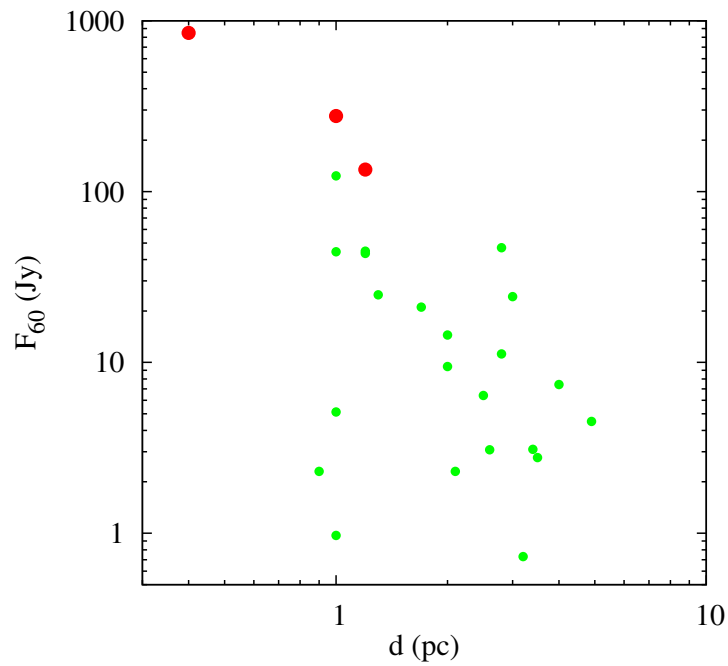
Figure 3.1: Distance and apparent brightness obtained by IRAS 60 μm relation of bipolar PNe. The red circles are our target, and the others are bipolar PNe listed in Corradi & Schwarz (1995).

Table 3.2: Standard star list of MAX38

Object Name	RA (J2000)	Dec (J2000)	Class
VX Sgr	18 08 04.04831	-22 13 26.6327	RSG
WAql	19 15 23.347	-07 02 50.35	Stype AGB
V1185Sco	17 44 24.01	-31 55 35.5	OH/IR
Alpha Boo	14 15 39.67207	+19 10 56.6730	RGB

pergiant surrounded by a dust shell. The size of the shell was reported to be 60 mas by Greenhill et al. (1994), which is much smaller than the spatial resolution in this work. A S-type Asymptotic Giant Branch (AGB) start W Aql shows a very extended dust shell whose annulus are from 36 to 86 arcsec (Cox et al. 2012). However the shell is very cold and too faint and the shell cannot be observed by miniTAO/MAX38, so this star can be also regarded as a point source in this study. Although any infrared images of V1185 Sco with high spatial resolution have not reported in literature, the FWHM measured in our observations is almost consistent to the FWHMs of the other stars, indicating that this star is also a point like object. The PSF and photometry reference stars listed above are bright enough for the flux calibration, while three of them (VX Sgr, W Aql, and V1185 Sco) are known as variable stars.

According to Schaeidt et al. (1996) and Sloan et al. (2003), the standard star flux by ISO/SWS itself contains calibration errors from 10 to 30%. We consider the 20% calibration error as the typical value into our flux calibration. As the result, uncertainty of the standard star flux can be 28%, taking a square root sum with the possible flux variation, and we adopt the value of 30%.

To check this expectation the cross calibration of the standard stars has been carried out. All the calibrated fluxes of the standard stars obtained from 2010 May to 2012 Oct were consistent with the expected intrinsic flux within the 30% level. This demonstrates that our calibration method is reliable enough and these stars can be used as the standard stars with the uncertainness of 30%. We use the fluxes of the PSF reference stars as the photometric calibrator with an uncertainness of 30%.

3.2 Observation

Observations were carried out in May 2011 and Oct. 2012. Weather conditions were good and the perceptible water vapor was low enough to conduct observations at 30 μm at both observation runs. Especially the weather on May 27 2011
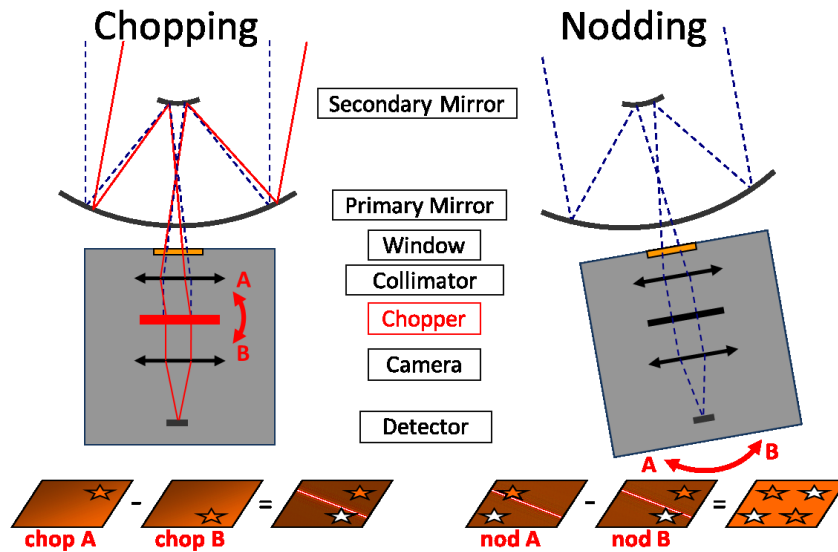
Figure 3.2: Schematic drawing of chop and nod observations of MAX38.

was excellent, enabling us to carry out long integration at the 37 μm. Details of the observations are summarized in Table.3.3 .

Since the thermal background from terrestrial atmosphere, telescope and instrument itself is much larger in the MIR wavelengths than the typical brightness of the targets, accurate subtraction of the background is critical. Standard chop and nod technique was applied for this study in a purpose of background subtraction. The chopping throw was 36 arcseconds for the observations of both NGC6302 and Hb5, and 42 arcseconds for Mz3. The frequency of the chopping was set to from 2.0 to 4.0 Hz which is faster than the typical timescale of the background fluctuation of 0.1 sec at 30 μm (see Uchiyama 2010). An internal chopping system mounted in the cold optics (4K) of the MAX38 camera was used for the chopping observations. This system enabled us to realize the fast chopping, but caused strong residual pattern on the subtracted images of two chopping beams. Nodding is a technique to cancel out the residual patterns by switching the telescope pointing with a frequency of 0.02 Hz. Fig 3.2 illustrates the observation scheme of the chop and nod technique. In Table 3.3, our observation parameter are shown.

Table 3.3: Observation logs

Object Name	Wavelength [μm]	OBS DATE	Integral time[s]
NGC6302	18.7	2012.10.25	500
NGC6302	31.7	2012.10.25	300
NGC6302	37.2	2011.5.27	5,000
Mz3	18.7	2011.5.28	400
Mz3	25.0	2012.10.21	1,000
Mz3	31.7	2011.5.28	3,000
Hb5	18.7	2012.10.20	500
Hb5	25.0	2012.10.20	900
Hb5	31.7	2012.10.24	3,000

Table 3.4: Observational conditions of standard stars with MAX38

Object Name	Wavelength [μm]	OBS DATE	Integral time[s]
Alpha Boo	18.7	2011.5.28	20
Alpha Boo	31.7	2011.5.28	1,000
V1185Sco	18.7	2011.5.28	20
V1185Sco	25.0	2011.5.28	100
V1185Sco	31.7	2011.5.28	100
V1185Sco	31.7	2012.10.24	200
V1185Sco	37.2	2011.5.27	500
VX Sgr	18.7	2012.10.25	100
VX Sgr	31.7	2011.10.25	400
VX Sgr	31.7	2012.10.24	400
WAql	18.7	2012.10.20	400
WAql	25.0	2012.10.20	1000

Chapter 4

Results

4.1 NGC6302

4.1.1 Images

Mid-infrared images of NGC6302 at 18.7, 31.7, and 37.2 μm obtained with mini-TAO/MAX38 are displayed in Figure 4.1. We note that the images at 31.7 and 37.2 μm have achieved the highest spatial resolution ever obtained and the extended structure seen at these wavelengths has been resolved for the first time. The presented images clearly show the extended structure, and the detailed characteristics are varied with the wavelengths. The images at 18.7 μm and 31.7 μm are slightly elongated to the north-south direction, while it shows relatively circular shape at 37.2 μm. A bright peak is seen around the center of the structure, and its position shifts with the wavelength. The peak is located at eastside of the center at 18.7 μm, at almost center at 31.7 μm, and at western-south side at 37.2 μm.

Figure 4.2, 4.3, 4.4 shows radial profiles of the object together with point spread functions (PSFs). The PSFs are measured from the standard star observations which were carried out before or after the target observations. VX Sgr was used for 18.7 and 31.7 μm, and V1185 Sco for 37.2 μm. Strictly speaking these stars are intrinsically not point sources, but the extension is expected to be much smaller than the current spatial resolution of 4.53 arcsec at 18.7 μm. The extended components are clearly detected in all wavelength. Evaluated full width half maximum (FWHM) is listed in Table 4.1.

The elongated structure seen at 18.7 μm was already reported in Kemper et al. (2002). They carried out an imaging observation of NGC6302 at 20 μm with ESO 3.6m telescope/TIMMI2. Figure 4.5 shows their image overlaid with the contour map of our image at 18.7 μm. The relative position is adjusted based on the centroids. Both images and its shapes give a good agreement, indicating that

[1] NGC6302 at 18.7 μm   [4] VX Sgr at 18.7 μm

[2] NGC6302 at 31.7 μm   [5] VX Sgr at 31.7 μm

[3] NGC6302 at 37.2 μm   [6] V1185 Sco at 37.2 μm
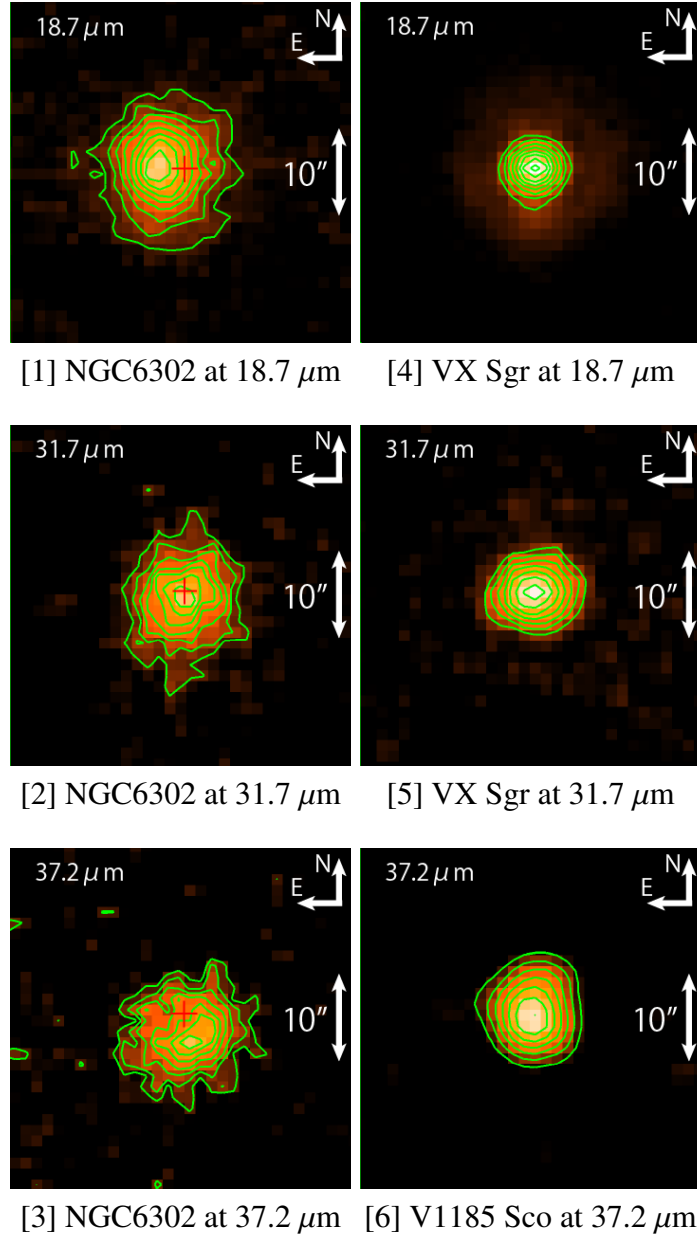
Figure 4.1: Mid-infrared images of NGC6302 obtained by MAX38. In the left row, images in 18.7, 31.7, and 37.2 μms are displayed with contours. In the right row, images of the PSF standard star are displayed in the same wavelength, respectively. A red cross indicates position of the central star reported by Szyszka et al. (2009)

[1] equatorial plane [2] lobe axis
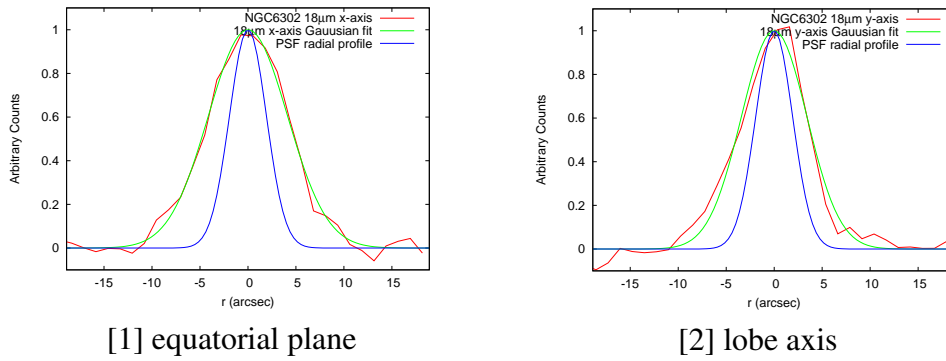
Figure 4.2: Radial profiles of NGC6302 along the lobe axis and the equatorial plane at 18.7 μm.

[1] equatorial plane [2] lobe axis
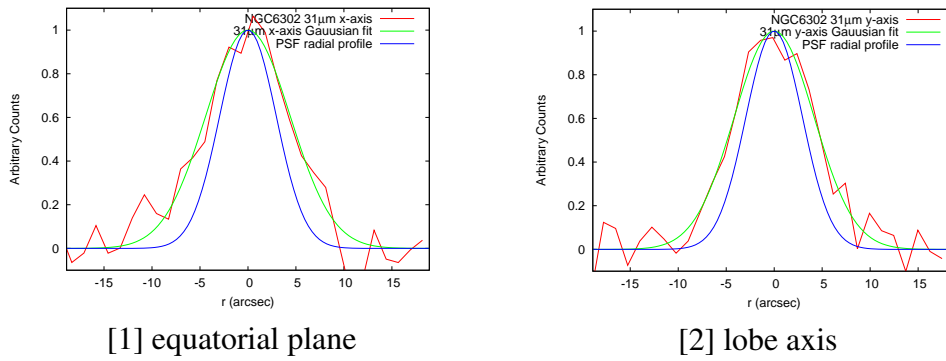
Figure 4.3: Radial profiles of NGC6302 along the lobe axis and the equatorial plane at 31.7 μm.

[1] equatorial plane [2] lobe axis
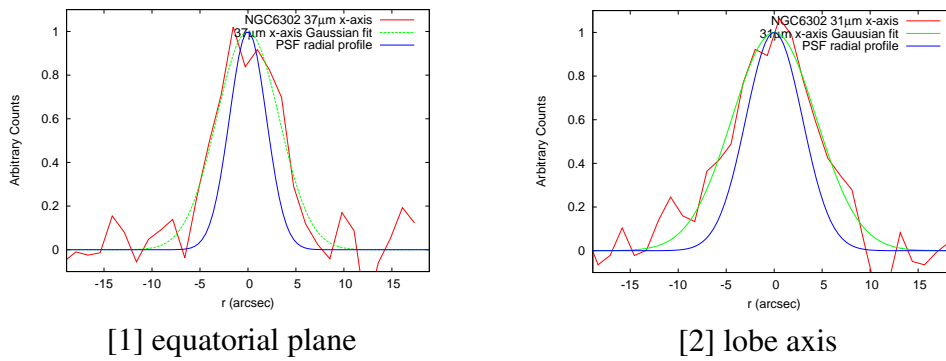
Figure 4.4: Radial profiles of NGC6302 along the lobe axis and the equatorial plane at 37.2 μm.

Table 4.1: Comparison of FWHM with NGC6302 and PSFs standard stars

Wavelength [μm]	Object Name	FWHM [arcsec]	PSF standard star Name	FWHM [arcsec]
18.7	NGC6302 equatorial	8.02 ± 0.33	VX Sgr	4.53 ± 0.06
18.7	NGC6302 lobe	9.68 ± 0.24	VX Sgr	4.53 ± 0.06
31.7	NGC6302 equatorial	9.77 ± 0.56	VX Sgr	6.93 ± 0.09
31.7	NGC6302 lobe	10.36 ± 0.68	VX Sgr	6.93 ± 0.09
37.2	NGC6302 equatorial	9.98 ± 0.80	V1185 Sco	7.37 ± 0.33
37.2	NGC6302 lobe	7.61 ± 0.68	V1185 Sco	7.37 ± 0.33
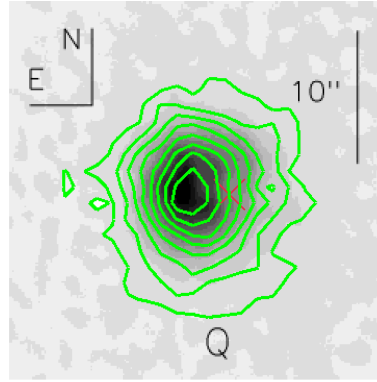
Figure 4.5: Contour map of our image of NGC6302 at 18.7 μm overlying on the image at 20 μm obtained of TIMMI2 (Kemper et al. 2002). A red cross indicates position of the central star reported by Szyszka et al. (2009)

the position is reasonably well adjusted.

A visible image with an excellent spatial resolution was provided by the Hubble Space Telescope / WFPC2. Figure 4.6, 4.7, and 4.8 display the HST image together with the contour maps of our mid-infrared images. The accuracy of the position adjustment is estimated as less than 4 arcsec in consideration with the stability of the telescope and the camera. At 18.7 μm the brightness peak is not located at the center of the dark lane seen in the optical image, but at the eastern part of the nebula. This suggests that the dense region seen as the dark lane in the optical image cannot be seen through even at 18.7 μm. The optical depth of the dark lane is therefore estimated to be larger than unity. Matsuura et al. (2005) pointed out that the extinctions within the disk is $A_{H\alpha}$ = 5–7 magnitude. On the other hand the structure seen at 37.2 μm traces the optical dark lane well, suggest-
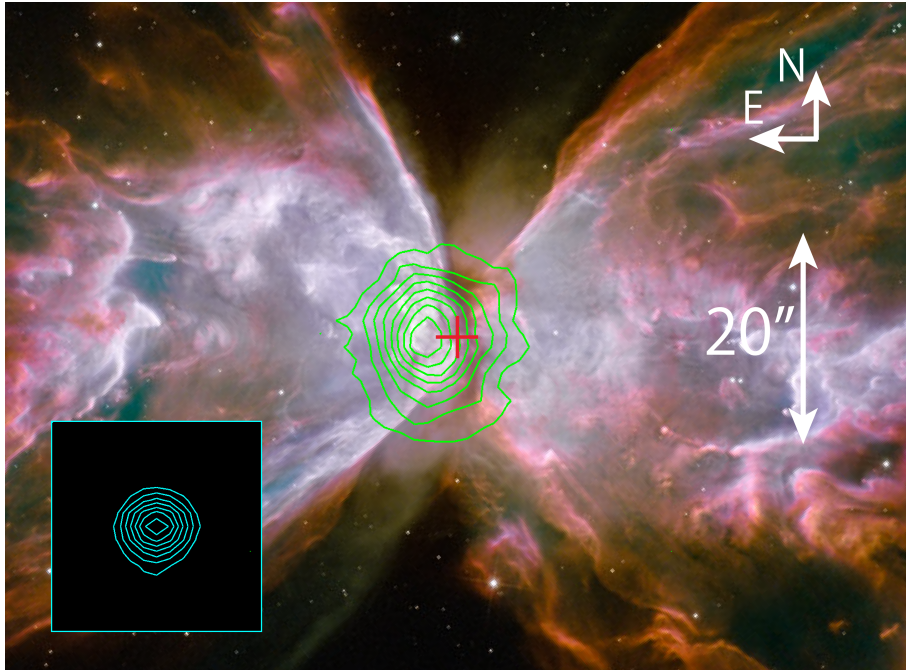
Figure 4.6: NGC6302 18.7 μm contour image (solid contours) obtained by MAX38 overlaid upon HST/WFPC2 with false color image. This contour is displayed with 30%, 40%, 50%, 60%, 70%, 80% and 90% levels of the 18.7 μm image. A lower left contour map is (PSF) standard star VX Sgr image level.

ing that the flux at 37.2 μm comes from the dust in the dark lane. The peak at 31.7 μm is located at the position of the central star detected by Szyszka et al. (2009), but we do not consider that the emission at 31.7 μm comes from the star itself or extremely central region.

4.1.2 Photometry and SED

Standard aperture photometry was applied for flux measurements. The aperture radii were set to twice of FWHM of standard star PSF, as 8.0, 12.0, and 13.0 arcsec at 18.7, 31.7, and 37.2 μm, respectively. Relation photometric error was estimated from the standard deviation of the blank sky area. Their absolute flux is calibrated by the photometry of VX Sgr at 18.7 and 31.7 μm and V1185 Sco at 37.3 μm. The uncertainty of the absolute flux are expected to be less than 30% (See Section 3.1). This dominates the error of the measurements.

The measured flux is 100 ±21 Jy, 430±130 Jy, and 700 ±320 Jy at 18.7, 31.7, and 37.3 μm, respectively. These values are almost consistent with the flux mea-
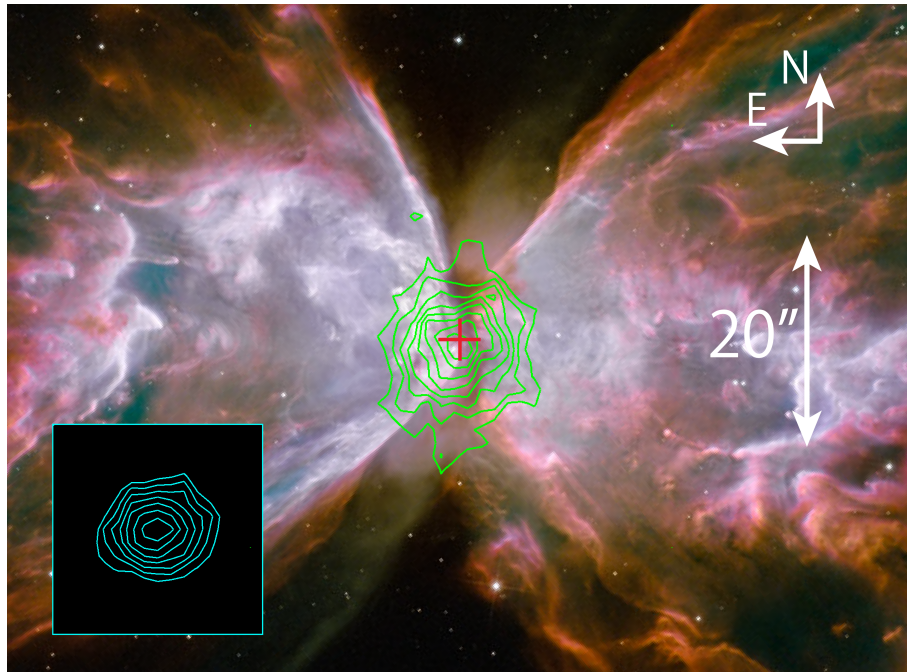
Figure 4.7: NGC6302 31.7 μm contour image (solid contours) obtained by MAX38 overlaid upon HST/WFPC2 with false color image. This contour is displayed with 30%, 40%, 50%, 60%, 70%, 80% and 90% levels of the normalized Gussian filter used to smooth the 31.7 μm image. A lower left contour map is PSF standard star VX Sgr image level.
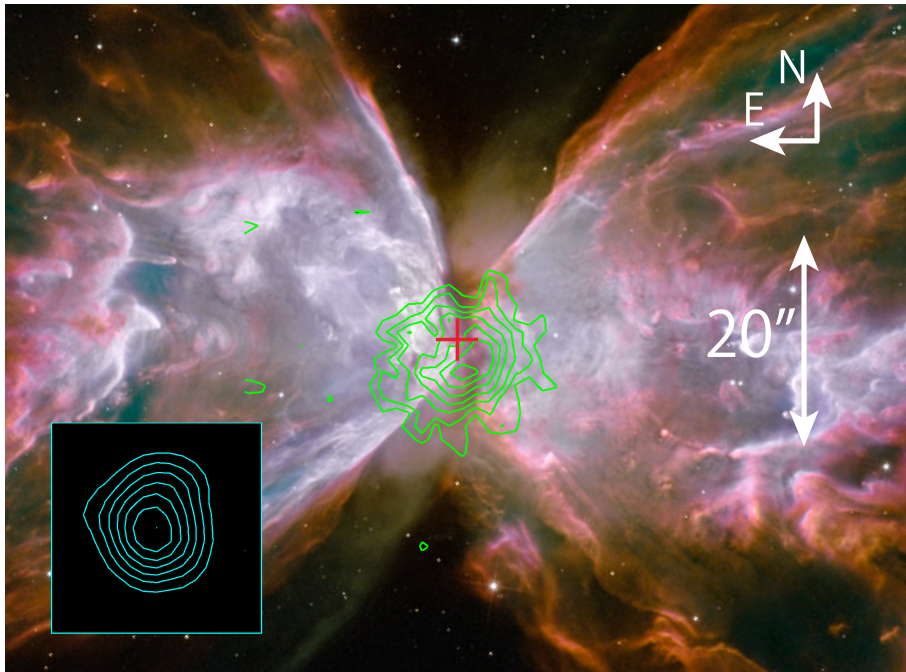
Figure 4.8: NGC6302 37.2 μm contour image (solid contours) obtained by MAX38 overlaid upon HST/WFPC2 with false color image. This contour is displayed with 30%, 40%, 50%, 60%, 70%, 80% and 90% levels of the normalized Gussian filter used to smooth the 37.2 μm image. A lower left contour map is PSF standard star V1185 Sco image level.

sured from the ISO/SWS spectrum over 1-sigma level. This suggests that approx-
imate 90% of the mid-infrared flux measured by the ISO/SWS comes from the
central region, and the contribution of the extended nebula is less than 10% in
these wavelengths. No other point-like sources detected within 161×150 arcsec^2
area.

The flux at 18.7 μm may be contaminated with the emission of [SIII] at 18.7 μm.
The intensity of the emission is measured as 150 W/m^2 by ISO/SWS but the spa-
tial distribution is not clear. Persi et al. (1999) pointed out that high-excitation
emission lines of [NeV] (14.32 μm) and [NeIII] (12.81 μm) concentrate around
the central star. If all the emission come from the central region, the contribution
of these lines to the present flux at 18.7 μm is estimated to be approximately 6%.
We estimate the flux comes from dust emission at 18.7 μm is 94 Jy.

Figure 4.9 shows the spectral energy distribution (SED) of the central region
of the nebula. The SED indicate existence of more than a single dust component.
We adopt a two component dust model with component A at a dust temperature
T_1 and component B at T_2 discribed as eq 4.1. We also assumed emissivity of λ^{-1}
in the fitting.

$$F(\lambda) = \frac{1}{\lambda} \frac{2hc^2}{\lambda^5} \left\{ \frac{A}{e^{\frac{hc}{\lambda k T_1}} - 1} + \frac{B}{e^{\frac{hc}{\lambda k T_2}} - 1} \right\} \qquad (4.1)$$

The best-fit SED plot is shown in Figure 4.9. The red circle represents the flux
from our observations. The red and blue square represent the flux obtained by
TIMMI2 and IRAS, respectively. The solid light blue line represents the ISO/SWS
spectrum line. Derived dust temperatures of the warm and the cold components
are 180 ± 50 and 70 ± 10 K, respectively. There are plotted as red and blue dot-
ted lines. The reduced χ^2 value of the fitting is 0.2, suggesting that the model
is reasonably fits the photometry data. The luminosity of the warm and the cold
components are estimated as 500 L$_\odot$ and 2900 L$_\odot$ respectively under an assump-
tion of the distance of 1.2 kpc.

A similar model was applied for the fitting of the mid- to far-infrared spectrum
obtained with ISO/SWS by Kemper et al. (2002). They suggested that the infrared
emission can be represented with the warm (100–118 K) and the cold (30–60 K)
dust components. These values are slightly lower than our results. These different
results may indicate the existence of colder dust.
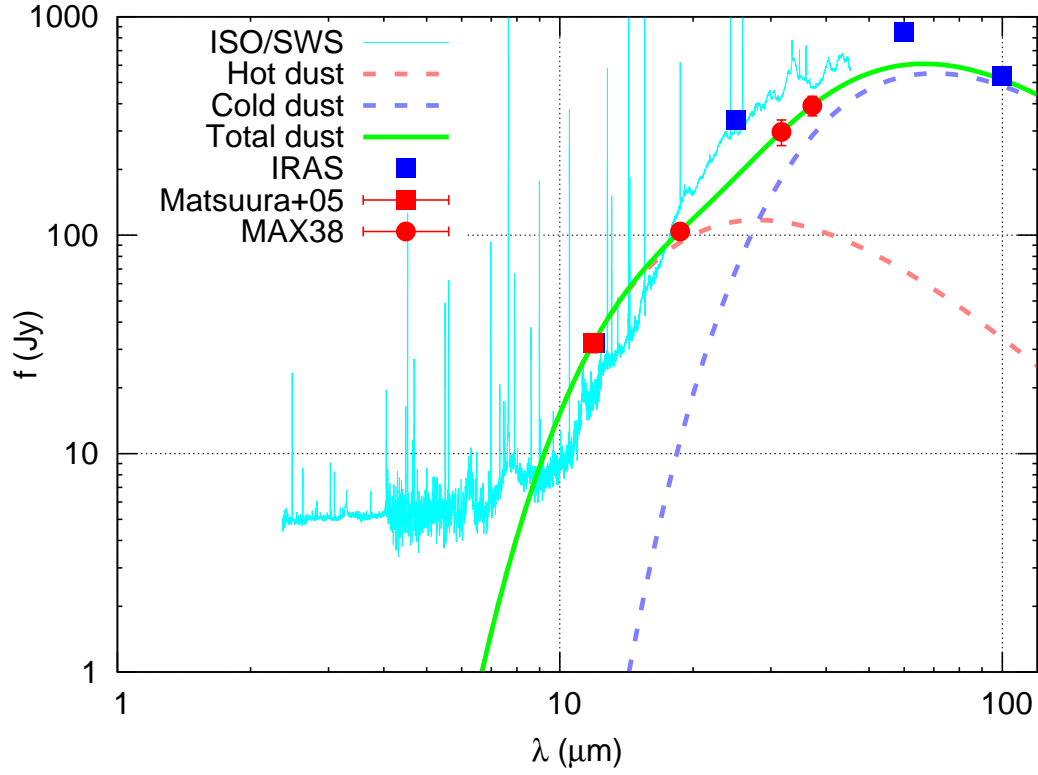
Figure 4.9: SED of NGC6302. See text for details.

Table 4.2: The fluxes of NGC6302 central region obtained by MAX38

Wavelength [μm]	Object name	Central region flux [Jy]
18.7	NGC6302	100±20
31.7	NGC6302	430±130
37.2	NGC6302	700±320

Table 4.3: FWHM of Mz3 and PSF standard stars

Wavelength [μm]	Object name	FWHM [arcsec]	PSFs name	FWHM [arcsec]
18.7	Mz3 equatorial	8.02 ± 0.33	WAql	4.53 ± 0.06
25.0	Mz3 equatorial	9.77 ± 0.56	WAql	6.93 ± 0.09
37.2	Mz3 equatorial	9.98 ± 0.80	VX Sgr	7.37 ± 0.33

4.2   Mz3

4.2.1   Images

Mid-infrared images of Mz3 at 18.7, 25.0, and 31.7 μm are displayed in Figure 4.10. All images show clearly resolved circumstellar shells and look similar to each other. They consist of three components, a central bright core and filamentary extended structures in the north and south direction .These structures are quite similar to the bipolar nebula seen in the visible image. Figures 4.11 show contour maps of the mid infrared images on an optical image obtained by HST/WFPC2. The position is adjusted based on the centroid of the core. These structures at 17.0 μm have already been reported in Smith & Gehrz (2005), but this is the first spatially resolved image at the longer (infrared) wavelengths. The detection of the central core at 25.0 and 31.7 μm is a surprising fact. Previous studies Smith & Gehrz (2005) with their shorter 17.0 μm wavelength images predicted that the central region of the Mz3 is too dim to be detected at these longer mid-infrared wavelengths. Our result suggests the existence of the cold (and may be massive) dust nearby the star. Detailed discussions will be given in the Chapter 5.

The central core seems to be a very compact source in all the wavelengths. The radial profile of the core is plotted in Figure 4.14, 4.15. For comparison point spread functions (PSFs) measured from the standard star V1185 Sco are also shown. The radial profile of the core is extended more than PSFs at all observed wavelengths, indicating that emission sources extend along its equatorial plane.

4.2.2   Photomety and SED

The total flux including the central core and the nebula are measured with standard aperture photometry. The photometric aperture are set to be 30 arcsec in diameter for all the images. The center of the aperture is at the central core. The absolute flux was calibrated with the photometry of V1185 Sco. The measured flux is 330 ± 70, 340 ± 70 , and 380 ± 90 Jy, at 18.7, 31.7 and 37.2 μm, respectively, which are slightly brighter than MIR flux obtained from ISO/SWS spectroscopic

[1] Mz3 at 18.7 μm [4] WAql at 18.7 μm

[2] Mz3 at 25.0 μm [5] WAql at 25.0 μm

[3] Mz3 at 31.7 μm [6] VX Sgr at 31.7 μm
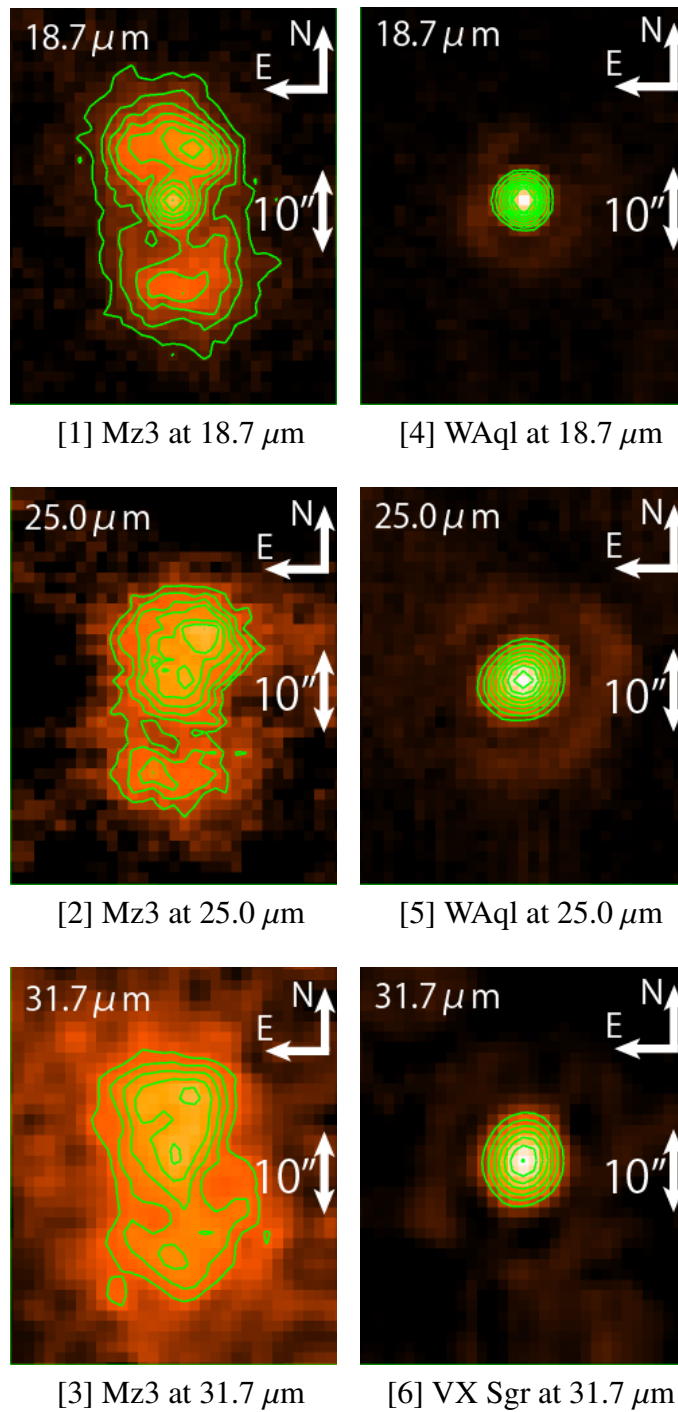
Figure 4.10: Mid-infrared images of Mz3 obtained by MAX38. In the left row, images in 18.7, 25.0, and 31.7 μms are displayed with contours. In the right row, images of the PSF standard star are displayed in the same wavelength, respectively.
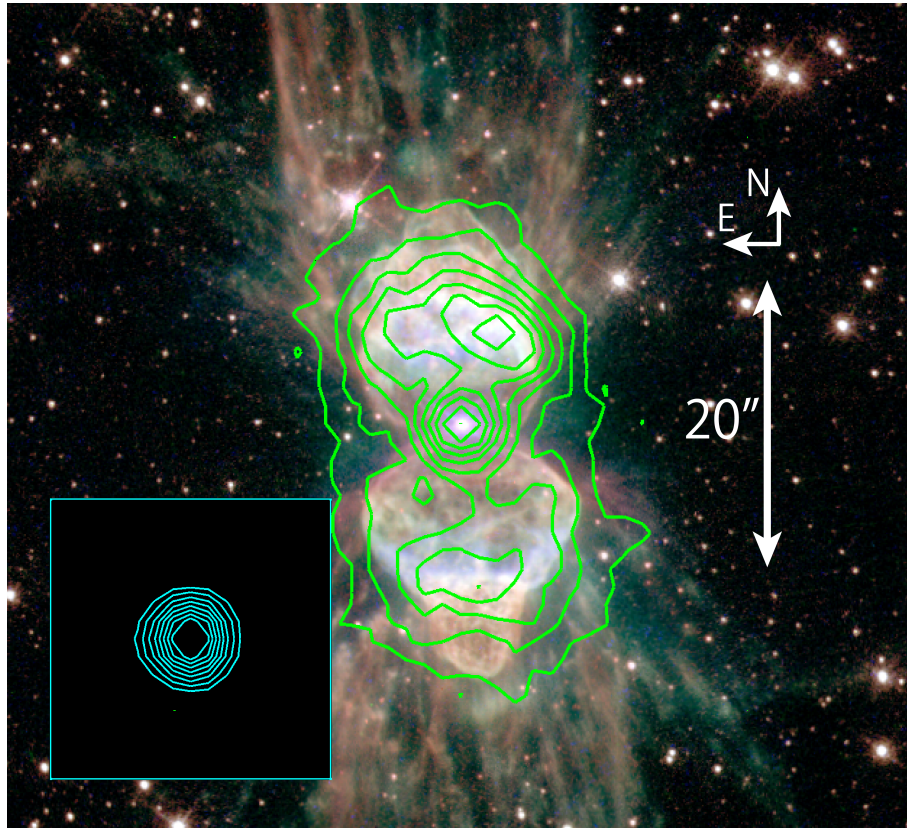
Figure 4.11: Mz3 18.7 μm contour image (solid contours) obtained by MAX38 overlaid upon HST/WFPC2 (with false color) image. The contour is displayed 18.7 μm image with 30%, 40%, 50%, 60%, 70%, 80% and 90% levels of the peak flux. A lower left contour map is PSF standard star WAql image level.

observation, 230, 250, and 280 Jy at 18.7, 25.0, and 31.7 μm in 1-σ level (See Table 4.4).

Contamination of [SIII] line at 18.71 μm to the flux at 18.7 μm should be considered. The contribution to the present flux at 18.7 μm is estimated to be approximately 6%. Smith & Gehrz (2005) reported the image of [NeII] line at 12.81 μm and suggested that the most of the emission come from the nebula region. Since the excitation potential of [SIII] (23.33eV) is almost similar to that of [NeII] (21.56eV), both lines are expected to emit at the similar locations, i.e., the nebula. This indicates that the contamination of the [SIII] can be neglected for the flux measurement of the central region.

Flux of the central core is measured with a PSF photometry. The PSF extracted from the image of V1185 Sco is adopted for the photometry. The measured flux is
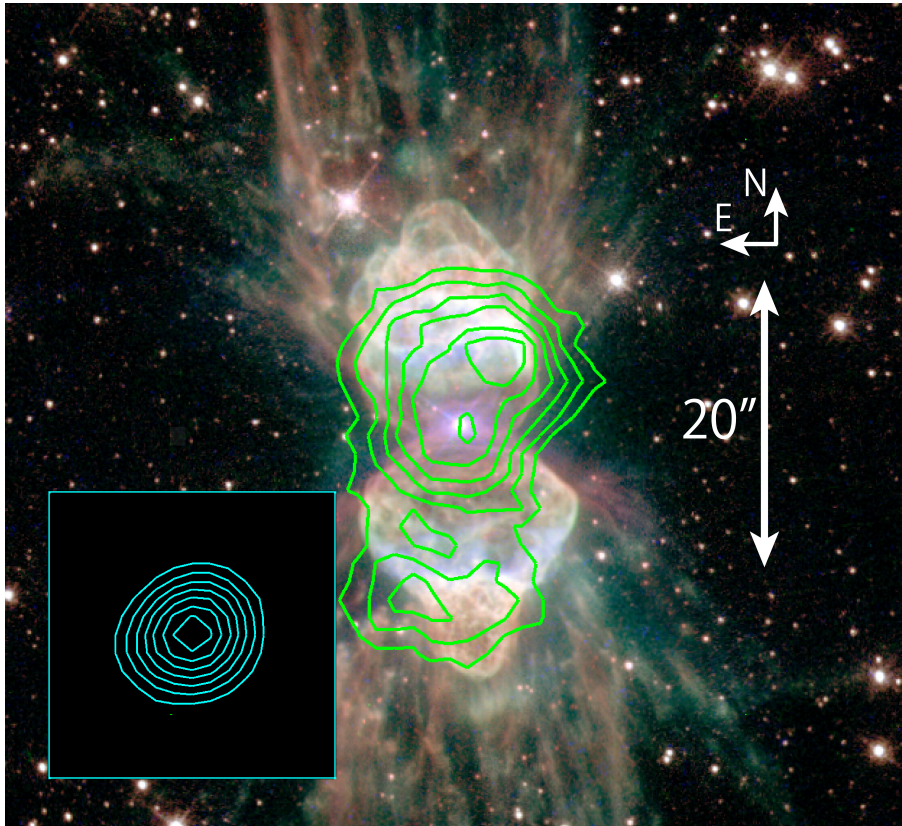
Figure 4.12: Mz3 25.0 μm contour image (solid contours) obtained by MAX38 overlaid upon HST/WFPC2 with false color image. This contour is displayed with 30%, 40%, 50%, 60%, 70%, 80% and 90% levels of the normalized Gussian filter used to smooth the 25.0 μm image. A lower left contour map is PSF standard star WAql image level.
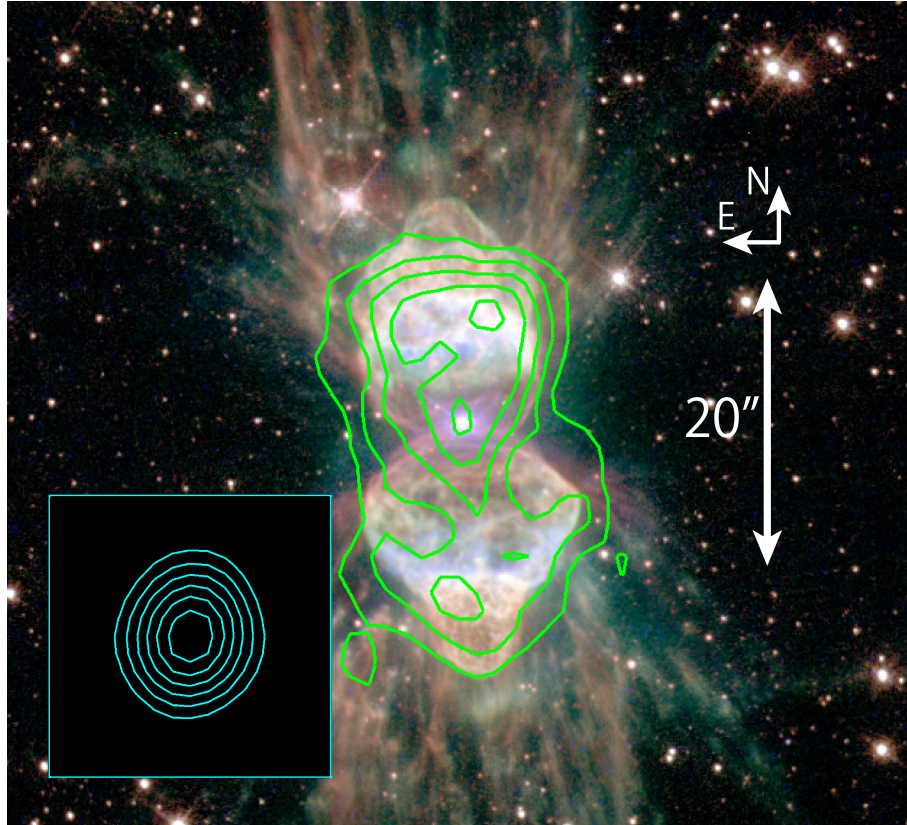
Figure 4.13: Mz3 31.7 μm contour image (solid contours) obtained by MAX38 overlaid upon HST/WFPC2 with false color image. This contour is displayed with 30%, 40%, 50%, 60%, 70%, 80% and 90% of the peak flux. A lower left contour map is PSF standard star VX Sgr image level.
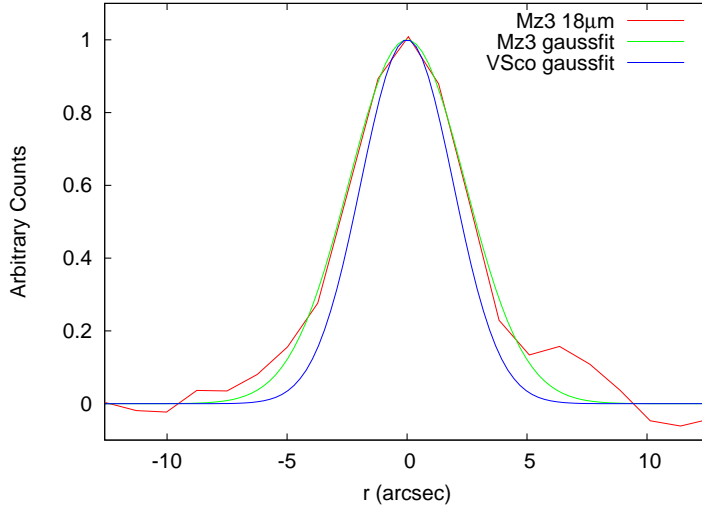
Figure 4.14: A projection of Mz3 along equatorial plane with 18.7 μm

60 ± 10, 120 ± 20, and 160 ± 40, at 18.7, 25.0, 31.7, and 37.2 μm, respectively, as listed in Table 4.4. These results suggest that more than one third of the total MIR fluxes of Mz3 comes from the central region. This is approximately three times brighter than the flux expected in previous observations at the shorter wavelengths (Smith & Gehrz 2005).

Figure 4.17 shows the SEDs obtained in this study. The fluxes of the whole nebula and the central core are displayed as the green circles and the red circles, respectively. The red and the blue squares represent the flux obtained by Smith & Gehrz (2005) and IRAS. The light solid blue line indicates the fluxes measured with a large aperture of ISO/SWS. The SED of the central core seems not to be fitted by single dust component, so we use two dust components with dust emissivity of λ^{-1} as described in Equation 4.1 for the fitting. The best-fit model SED is plotted as a solid curve in Figure 4.17. Derived dust temperatures of warm and cold components are 480 ± 20 and 90 ± 10 K, respectively. The reduced χ^2 value of 0.2 suggests that this fitting model explains the observed flux well. The luminosity of the central core estimated from our results is 1180 $L_{\odot}$ in total, and the warm and the cold components have 500 $L_{\odot}$ and 680 $L_{\odot}$, respectively.

Smith & Gehrz (2005) also claimed that there are two dust components in Mz3. One is the warm component of 320 K located in the central region, and the other is the cold dust of 110 K existed in only the nebula. Our result clearly suggests the existence of the cold dust at the central region in addition to the warm dust component.
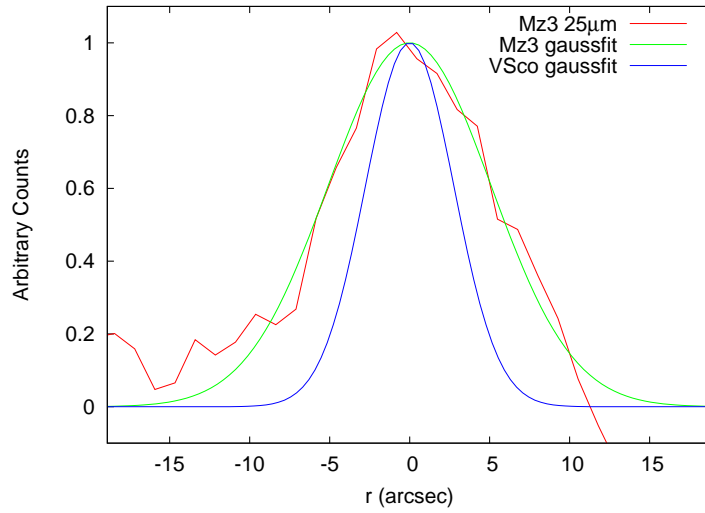
Figure 4.15: A projection of Mz3 along equatorial plane with 25.0 μm

Table 4.4: The fluxes of central region and all region obtained by MAX38

Wavelength [μm]	Object name	Total flux [Jy]	Central region flux[Jy]
18.7	Mz3	330±70	60±10
25.0	Mz3	340±70	120±20
31.7	Mz3	380±90	160±40
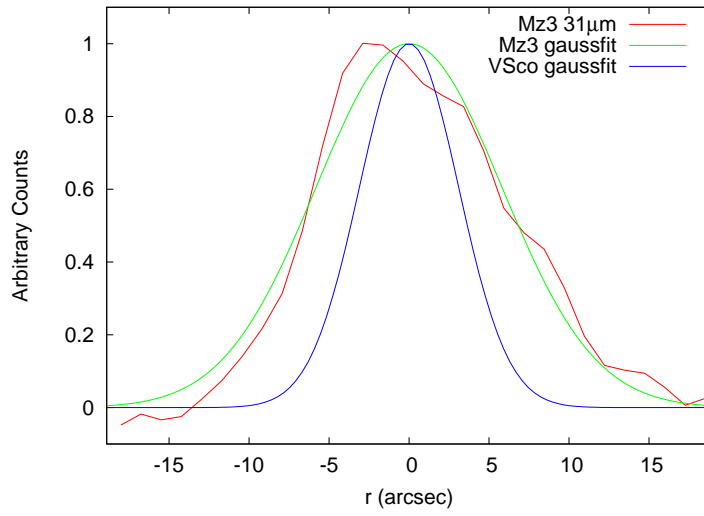
Figure 4.16: A projection of Mz3 along equatorial plane with 31.7 μm
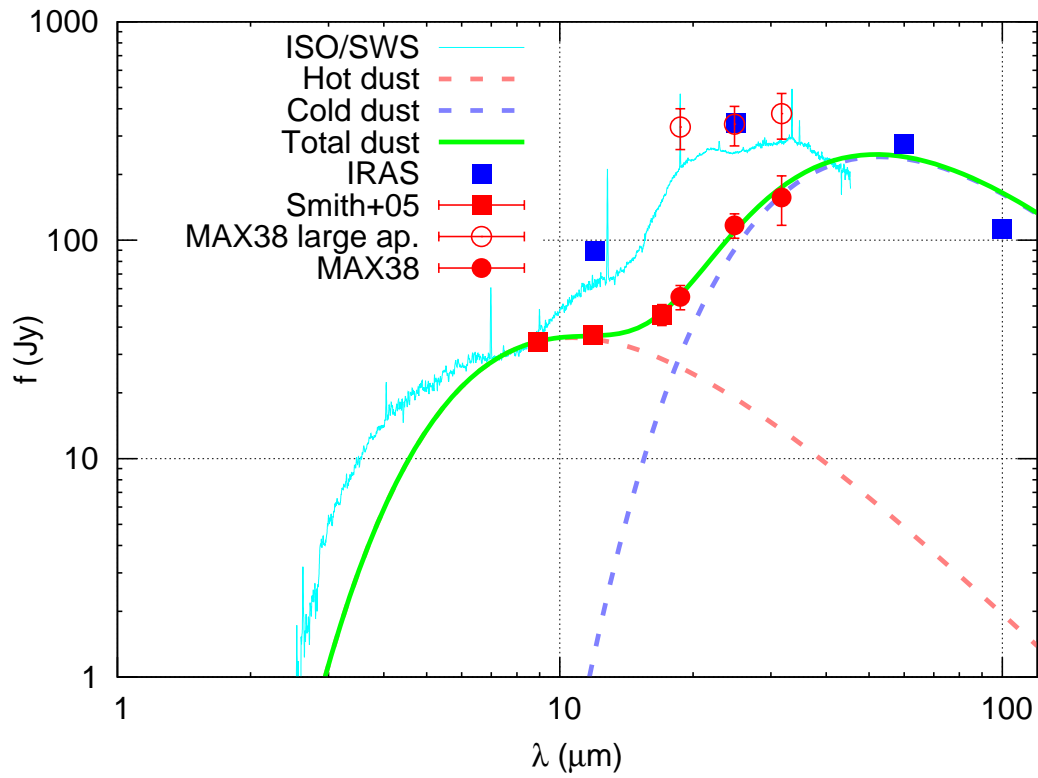
Figure 4.17: SED of Mz3

Table 4.5: FWHM of Hb5 and PSF standard stars

Wavelength [μm]	Object name	FWHM [arcsec]	PSFs name	FWHM [arcsec]
18.7	Hb5	6.51 ± 0.18	WAql	4.53 ± 0.06
25.0	Hb5	6.90 ± 0.12	WAql	5.92 ± 0.06
31.7	Hb5	8.11 ± 0.24	VX Sgr	6.93 ± 0.09

Table 4.6: The fluxes of Hb5 central region obtained by MAX38

Wavelength [μm]	Object name	Central region flux [Jy]
18.7	Hb5	31±7
25.0	Hb5	85±20
31.7	Hb5	85±30

4.3   Hb5

4.3.1   Images

Mid-infrared images of Hb5 at 18.7, 25.0, and 31.7 μm obtained with mini-TAO/MAX38 are displayed in Figure 4.18. These images show that the object is generally compact and slightly extend at all wavelength. The radial profiles are displayed in Figure 4.19, 4.20, and 4.21.

4.3.2   Photomety and SED

Standard aperture photometry was also applied to Hb5 with the aperture radii of 8.0 arcsec, 11.0 arcsec, and 13.0 arcsec at 18.7, 25.0, and 31.7 μm which correspond with twice as large as FWHM of the PSF standard star image, respectively. Absolute flux was calibrated with the photometry of the star VX Sgr. We mention again that the uncertainty of the absolute flux are expected to be less than 30% (See Section 3.1). This dominates the error of the measurements.

The measured absolute flux of Hb5 is 31 ± 7 Jy, 85 ± 20 Jy and is 85 ± 30 Jy at 18.7, 25.0, and 31.7 μm, respectively, as in Table 4.6. These values are consistent with the flux measured by ISO/SWS, 37, 86, and 100 Jy at 18.7, 25.0, and 31.7 μm, respectively, in 1-sigma level. This agreement suggests that most of the MIR fluxes of Hb5 come from the central region. We note that 18.7 μm flux contains [SIII] emission line, and that 25.0 μm flux contains [NeV] and [OIV] emission lines. In case that the most of line fluxes come only from central region of Hb5, as

[1] Hb5 at 18.7 μm

[4] WAql at 18.7 μm

[2] Hb5 at 25.0 μm

[5] WAql at 25.0 μm

[3] Hb5 at 31.7 μm

[6] VX Sgr at 31.7 μm
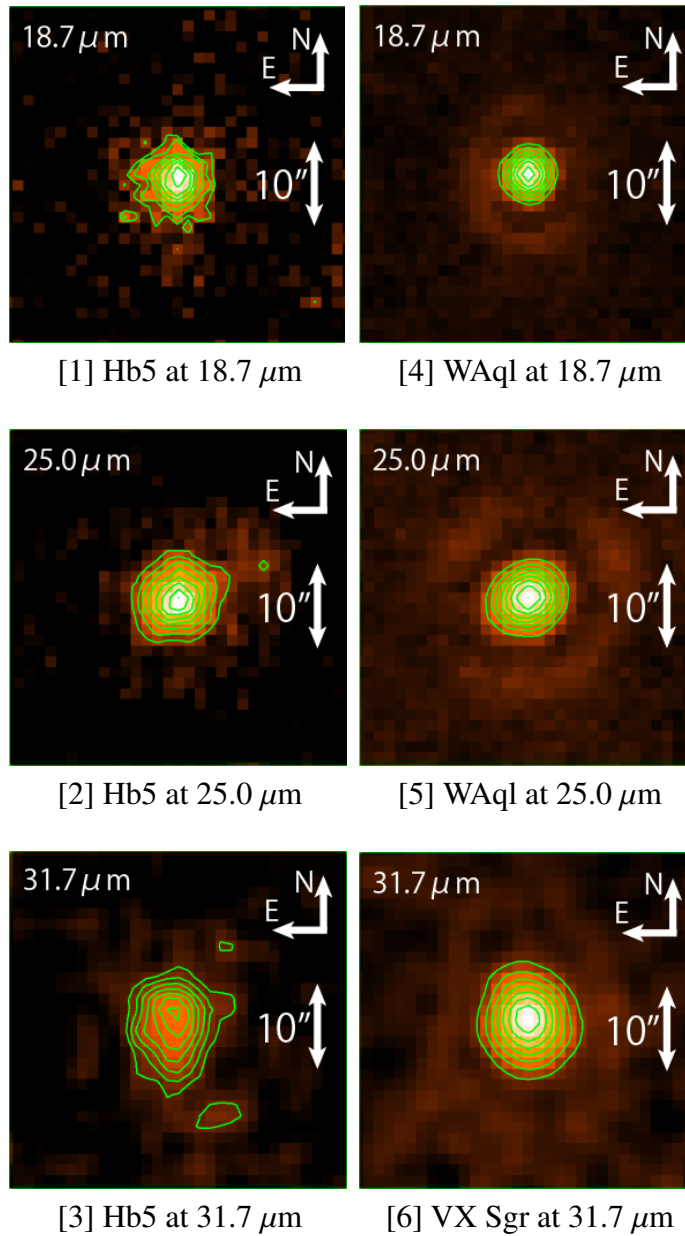
Figure 4.18: Mid-infrared images of Hb5 obtained by MAX38. In the left, images in 18.7, 25.0, and 31.7 μms are displayed with contours. In the right, images of the PSF standard star are displayed in the same wavelength, respectively.
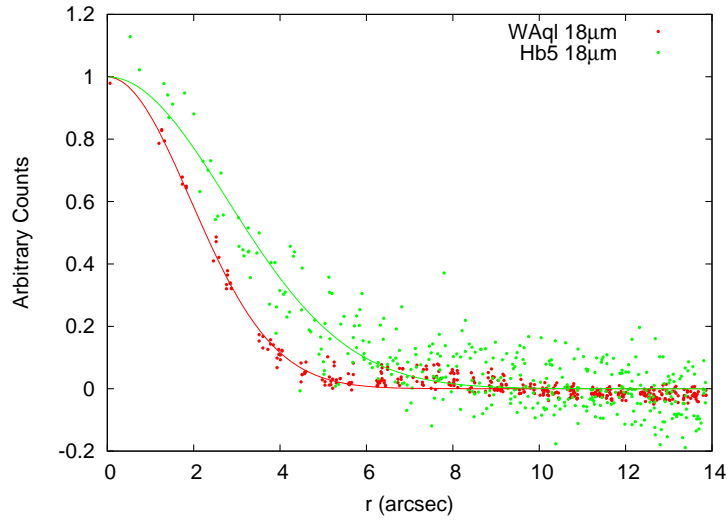
Figure 4.19: A radial profile of Hb5 at 18.7 μm

reported by Pottasch & Surendiranath (2007), their contribution to 18.7 μm flux and 25.0 μm flux are about 7 and 29%, respectively. We employ the flux comes from only dust emission at 18.7 and 25.0 μm is 30 and 60 Jy, respectivelyxsxc.

Figure 4.22 shows SED of Hb5 obtained by MAX38 observation plotted with ISO/SWS spectrum archive data. The red circle represents the flux obtained in this study. The blue squares represent the IRAS flux. The solid light blue and a solid green line represent the ISO/SWS spectrum and best fit SED based on our photometry results.

The SED seems to be fitted with single dust component. We fit the SED at central region with one dust temperature component. As shown in figure 4.22, the derived temperatures is 120 ± 20 K with reduced χ^2 value of 0.03 , and dust luminosity is 340 L$_\odot$ under an assumption of the distance of 1.4 kpc (Rice et al. 2004). At longer wavelength IRAS fluxes may indicate an existence of colder dust.
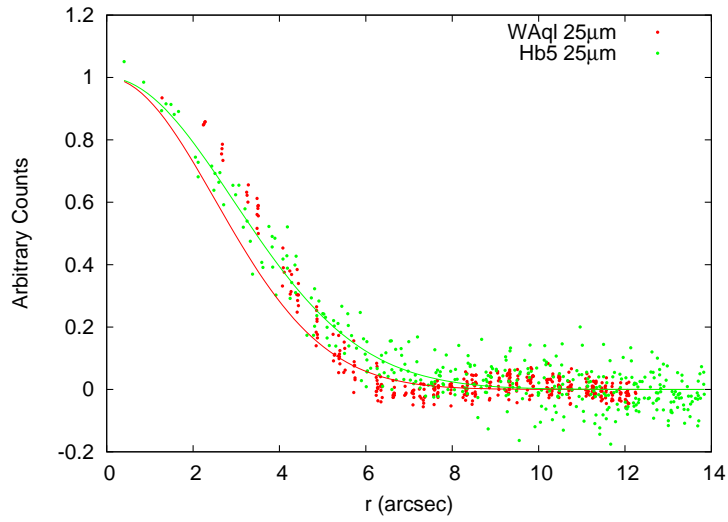
Figure 4.20: A radial profile of Hb5 at 25.0 μm
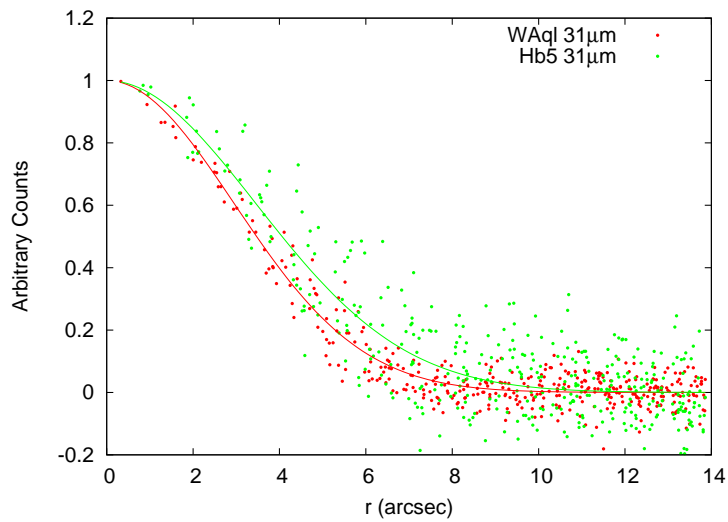
Figure 4.21: A radial profile of Hb5 at 31.7 μm
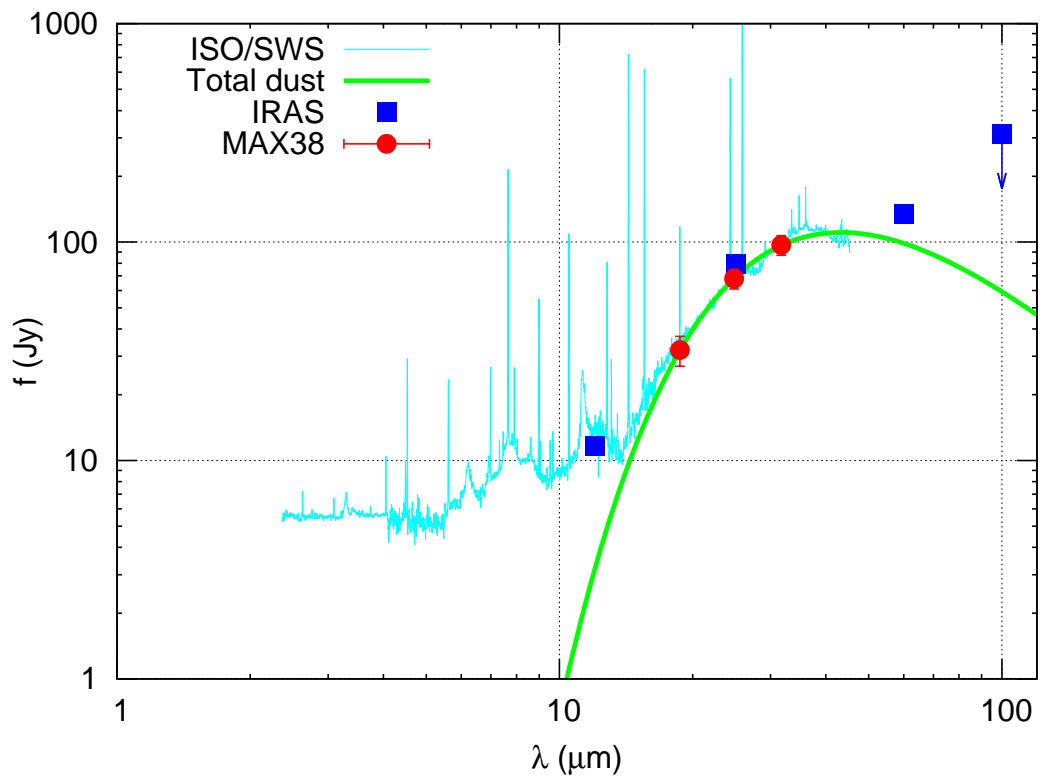
Figure 4.22: SED of Hb5. See text for details.

Chapter 5

Discussion

5.1 Dust Mass Estimation

In this section, we estimate the mass of cold dust component which we found on the SEDs in mid-infrared wavelengths. Such cold dust may be expected to exist in an optically thick structure. However, we employ here the optically thin dust in the mass calculation for simplifying the calculations, in purpose of understanding the basic structure of dust torus without complicated assumptions. Under this situation, the derived dust mass should be the lower limit.

A spherical dust grain with a radius a radiates a gray-body, whose luminosity l is written as

$$l = 4\pi a^2 < Q > \times \sigma_* T^4 \tag{5.1}$$

where σ_* is Stefan-Boltzmann constant, and T is dust temperature, and $< Q >$ is the emissivity averaged over the emitted wavelength.

If the dust emission is optically thin, a total number of dust grain can be derived by dividing total dust luminosity L_d by the luminosity of unit dust mass l. Therefore the total dust mass can be calculated as

$$M_d = \frac{4}{3}\pi a^3 \times \rho \times \frac{L_d}{l} = \left(\frac{a\rho}{3Q\sigma_* T^4}\right) L_d \tag{5.2}$$

where ρ is the mass density of the dust grain. The emissivity $< Q >$ strongly depends on the dust model. Two dust models are adopted in this study. One is given by Gilman (1974). This is a very classical model but is very useful because the emissivity in this model is proportional to the dust radius a and M_d becomes independent to a. The other model is Draine & Lee (1984), which is one of the most commonly used dust models. In this case the dust radius is assumed to be 0.1 μm which is the typical size of the interstellar grain. It is noteworthy that the emissivity of Draine & Lee (1984) is systematically lower than that of Gilman (1974), causing the lower dust mass by an order of magnitude.

Table 5.1: Calculation parameters of dust mass estimation

Object name	Distance [kpc]	Temperature [K]	Luminosity [$L_\odot$]	Composition	Dust density [g/cm^3]
NGC6302	1.2	70	1,200	C	2.25
Mz3	1.3	90	680	O	2.70
Hb5	1.4	120	4,000	C	2.25

Dust component is another issue to be determined the dust emissivity. In NGC6302 Kemper et al. (2002) found that the dust shows dual chemistry of silicate and carbonaceous dust. They claimed that the lower temperature component (30–60 K) contains silicates, water ice and carbonates and that the higher temperature component (100–118 K) contains only featureless carbonaceous dust. Temperature derived in this study is 70K that approximately corresponds to the transient temperature. Recently, ALMA vividly showed the presence of atomic carbon gas in the dark lane region by their sub-mm observation[1], which suggests that the central region of NGC6302 is carbon-rich. Therefore carbonates graphite is applied to the calculation in the NGC6302 case.

The infrared spectrum of Mz3 obtained by ISO seems nearly featureless. Chesneau et al. (2007) carried out interferometric observations in the mid-infrared range and found that the visibility variation shows a weak silicate feature around 10 μm. They pointed out that the dust in the hot inner disk is dominated by silicates. Although this inner hot disk is different from the source of the cold dust component observed in this study, it is natural to assume silicate dust in this calculation. For Hb5 the dust composition may be regarded as carbonaceous graphite according to Peeters et al. (2002) who found PAH emission features on its ISO/SWS spectrum.

Parameters for the calculation and the derived results are summarized in Table 5.1 and 5.2, respectively. Note that the different dust composition only cause the change of the derived dust mass within a factor in the extreme case of pure silicate composition instead of pure graphite composition.

Similar estimations of the dust mass have been carried out in previous studies. Matsuura et al. (2005) conducted the sub-mm observation of NGC6302 and estimated the dust mass in the central region of the nebula to be 0.03 $M_\odot$. This gives a good agreement with our estimation with the Gilman (1974) model. If the emissivity of Draine & Lee (1984) is adopted, the dust mass derived in this study is factor of 10 smaller than the result of Matsuura et al. (2005). This could be

---

[1] ALMA press release Sep 02, 2013

Table 5.2: dust mass around PN central core

| Object name | Temperature [K] | Dust mass [$M_\odot$] | |
| | | Dust emissivity model | |
		Gilman1974	Draine1984
NGC6302	70	2.5×10^{-2}	2.5×10^{-3}
Mz3	90	2.2×10^{-3}	2.4×10^{-4}
Hb5	120	1.0×10^{-3}	8.0×10^{-4}

explained if a certain amount of dust stay in the outer cooled region in the nebula. Actually the far infrared spectrum obtained by ISO/SWS clearly shows a cooler component than 70K. The other explanation is that the dusty torus is totally optically thick. Since being optically thin at the infrared wavelengths is assumed in this model, the estimated mass listed in Table 5.1 gives lower limits as already mentioned. The optical thickness at the central region will be discussed in the following section again.

In Mz3 Smith & Gehrz (2005) presented the dust mass of $1.1 \times 10^{-6} M_\odot$. They carried out observation in the wavelengths shorter than 18.7 μm and derived the dust temperature as hot as 320K. It is clearly higher than our result, suggesting that they missed the cooler dust that is only able to be detected in much longer wavelength such as 31.7 μm. For Hb5 our result is the first report about the mass of cold dust. Our calculation showed that the dust mass is between 8.0×10^{-4} and $1.0 \times 10^{-3} M_\odot$.

5.1.1 Geometrical Structure of the Central Region

All of the observed objects have a clear bipolar structure in optical wavelengths. Images of [NII] and [OIV] (see Figure 4.6 and 4.11) show that highly-excited ionized gas spreads along the bipolar lobes over several thousand AU while it is obscured in the perpendicular direction. This strongly indicates that the ionizing UV emission from the central star can penetrate only in the polar directions. Such kind of obscuration of central star radiation can be explained by a disk-like or toroidal distribution of the matter around the central star, which is optically thick in UV. This should be the source of the strong mid-infrared radiation observed in this study.

Assuming that the disk or the torus is completely optically thick in UV and it is completely optically thin in the bipolar direction, opening angles of the dusty structure can be estimated by calculating the ratio of central star luminosity against cold dust luminosity. Here the opening angle θ is defined as an angle from the equatorial plane to the edge of the disk/torus. This ratio represents a propotion

of total flux from the central stars against infrared flux from the surrounding dust. The luminosities of central stars are collected from literature such as Szyszka et al. (2009), Smith (2003), and López et al. (2012). The luminosities of dust torus are calculated via the integration of the fitted SED to the cold dust component.

Table 5.3: Opening angle of Cold Dust Torus in bipolar PNe

Object name	Luminosity of cold dust torus [$L_\odot$]	Luminosity of CSPN [$L_\odot$]	Opening angle of torus [degree]
NGC6302	1,200	2,000[1]	50
Mz3	680	5,700[2]	20
Hb5	4,000	2,0000[3]	26

[1] Szyszka et al. (2009)
[2] Smith (2003)
[3] López et al. (2012)

The derived opening angles are 50, 20, and 26 degree for NGC6302, Mz3, and Hb5, respectively. These clearly indicate that the obscuring structures are NOT geometrically thin disks BUT geometrically thick tori. In addition, these large opening angles suggest that these are not long-lived, Keplerian rotational tori, because the scale height z of a Keplerian torus is generally smaller than its disk radius R(z≪R). Recently expanding gas around the central stars are detected in some bipolar PNe or post-AGB stars. Peretto et al. (2007) found the expanding CO gas along the equatorial plane in NGC6302 by SMA observations. Another example of the expanding torus is found in M2-9 reported by Castro-Carrizo et al. (2012). This is a bipolar PNe and called as "a twin of Mz3". A similar structure was reported in the Red Rectangle nebula. Bujarrabal et al. (2013) detected the expanding disk structure in the outer region of the equatorial plane in addition to the Keplerian gas disk at the inner region by IRAM interferometer and ALMA. Therefore it is natural that the dusty toroidal structures found in this study are expanding tori.

5.2   Radial Stnurcture of the Dusty Tori

Another important information derived from our observations is radial structure of the dusty tori. As mentioned in Chapter 4, all of the emitting regions are very compact even at 31.7 or 37.2 μm. This might be strange because cold dust naturally distribute far from the luminous central star. In this section we will discuss this issue with simple assumptions.

It is natural that the input and the output energy of the dust grains are balanced. Therefore the dust temperature in the dusty torus can be estimated by solving the

Table 5.5: The list of calculation results of thermal equilibrium temperatrue

Object name	Dust temperature [K]	Cold dust distance with DUSTY [AU]	Cold dust torus size with MAX38 [AU]
NGC6302	70	9,000	<4,100
Mz3	90	18,000	<4,300
Hb5	120	7,200	<3,000

thermal equilibrium if it is assumed to be optically thin in the optical and the UV wavelengths. A thermal radiation transfer code DUSTY (Ivezic et al. 1999) is used for this estimation. Here the following assumptions are adopted; i) the dust has a standard size distribution (density $\propto a^{-3.5}$ from 0.005 to 0.25 μm) which called NMR model, ii) the chemical composition of the dust is silicate for the cases of NGC6302 and Hb5, and graphite for Mz3 as discussed previously, iii) the stellar effective temperature is 50,000, 32,000, 230,000 K, NGC6302, Mz3, and Hb5 , respectively (Szyszka et al. 2009; Cohen et al. 1978; Rice et al. 2004). The estimated relations between the distance from the star and the dust temperature are displayed in Fig 5.1, 5.2, 5.3. The upper limit of the emitting region sizes are also shown in these figures.

Table 5.4: Calculation parameters with DUSTY

Object name	Effective temperature [K]	Composition	References
NGC6302	150,000	Carbonate	[1]
Mz3	32,000	Silicate	[2,3]
Hb5	230,000	Carbonate	[4]

[1] Szyszka et al. (2009)
[2] Smith & Gehrz (2005)
[3] Quinn et al. (1996)
[4] Rice et al. (2004)

Those model calculations give the torus size being approximately double dust of one derived as FWHM of central star flux distribution along equatorial plane in the 31.7 μm image by MAX38. Two possible situations can be accounted for our small cold dust torus. One is optically thick torus even in the infrared wavelength, the other is dust grain growth in the cold dust torus.
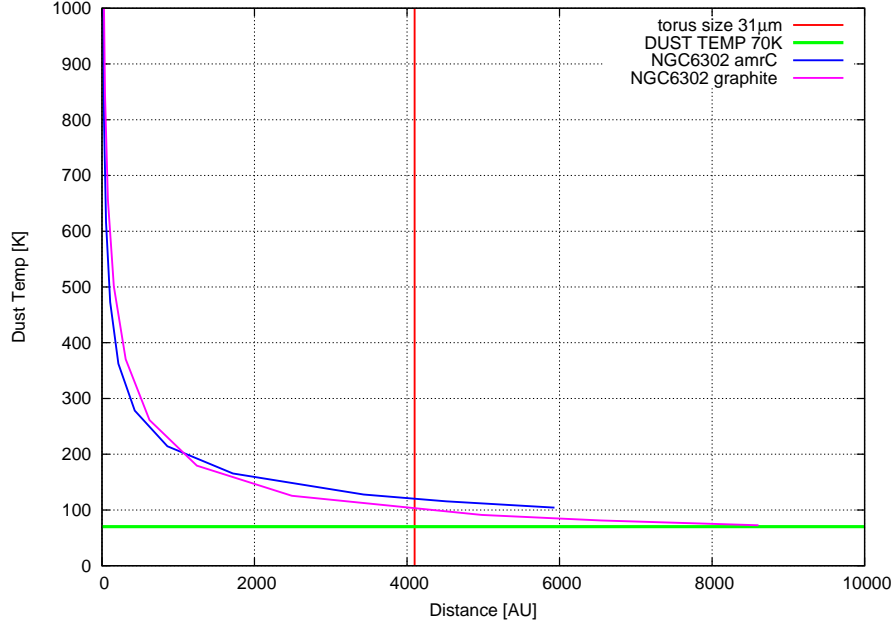
Figure 5.1: Thermal equilibrium temperatrue against a distance from central stars in NGC6302 calcurated by DUSTY.

5.2.1   Optical Thickness

If a certain amount of dust exists at the inner region of the dusty torus and effectively absorbs the radiation from the central star, the dust temperature at the outer region is expected to decrease. If this is the case, the dusty torus is optically thick in the optical and the UV wavelengths and the most of the stellar radiation is absorbed at the inner hot region. The absorbed energy of the stellar radiation should re-radiate in the near- or the shorter side of the mid-infrared wavelengths. However those warm components are not seen in the infrared SEDs of these objects. This is explained if the infrared radiation from the warm dust cannot penetrate through the outer torus. In other words, the dusty torus is expected to be totally optically thick at near and the shorter side of the mid-infrared wavelengths. Estimation of total mass of cold dust torus is very difficult due to uncertainty of its thickness. However, it can be stated that the dust mass is expected to be much heavier than our results in case of optically thick and cold dust torus.

This is supported by previous observations. Kemper et al. (2002) reported that the dark lane is seen around the central star in the image of NGC6302 at 18.7 μm. Chesneau et al. (2007) made a model of the inner disk structure for Mz3 and estimated that the optical depth at N-band of $\tau_N \sim 3.5$. We note that
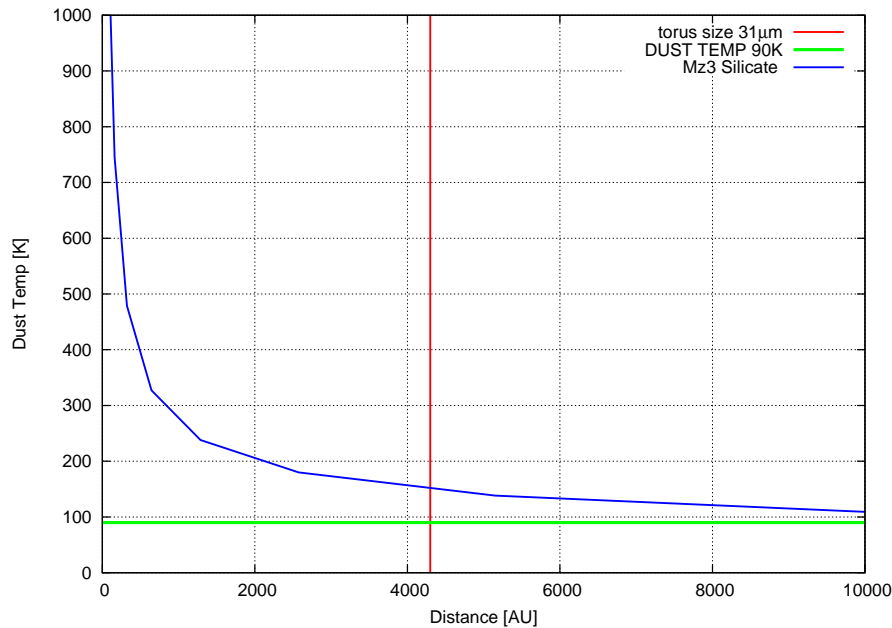
Figure 5.2: Thermal equilibrium temperatrue against a distance from central stars in Mz3 calcurated by DUSTY.

this explanation requires the inner region opening angle to be almost the same as that of the outer torus. If the inner region is geometrically thin (like flared disks commonly seen in young objects), some parts of the outer tori would be directly heated by the stellar radiation and detected in the mid-infrared wavelength. On the contrary if the inner region were geometrically thicker than the outer region, the radiation from the protruding region would also be detected. This may be a strong constraint on the radial structure of the dusty tori derived from this study.

Although the optically and the geometrically thick disk exists at the central region, it may be surprising that the central star can be seen at the center of the Mz3 even in optical wavelength. Cohen et al. (1978) has mentioned that this is the partially obscured central hot star with the spectral type of O9.5 ($\sim 32,000$ K). This dimmed emission from the central star can be also seen in the infrared SED of Mz3 obtained by Spizter.

This situation can be easily explained by the geometrical model. The inclination angle of the dust torus in Mz3 was estimated to be 74 degree by Chesneau et al. (2007). On the other hand the torus angle is derived as 20 degree by our observations. Therefore the line of sight to the central star intersects the dust torus at only 4 degrees apart from the rim. If the torus were a solid entity, the stellar light would be completely blocked. But practically the torus has density grada-
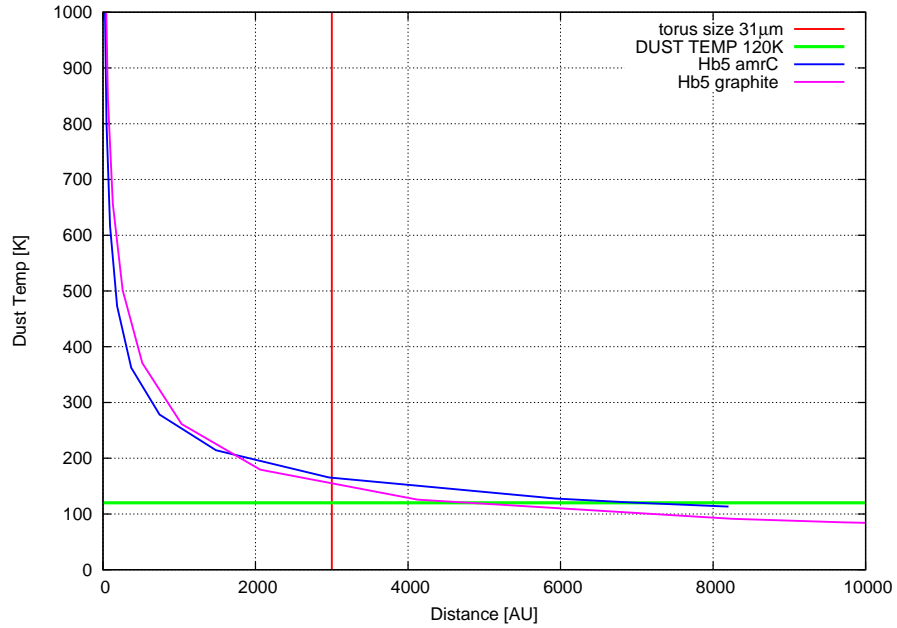
Figure 5.3: Thermal equilibrium temperatrue against a distance from central stars in Hb5 calcurated by DUSTY.

tion along the thickness of the torus, and the central star is observed as a partially obstructed object. Significant excess at the mid-infrared wavelengths in the SED of Mz3 may also indicate that the innermost and hottest dust is also seen through the relatively diffuse or patchy region around the rim of the dust torus.

On the contrary the central star of Hb5 is completely obscured, which suggests that this object is nearly face-on and the emission from the central star is totally absorbed by the thick dust torus. This gives a good agreement with the observational fact that the hot component from the innermost region is not seen in the infrared SED at all.

5.2.2   Dust Grain Growth

Another possible and reasonable explanation for the compact emitting region of the dust tori is the dust growth. The emissivity of dust grains strongly depend on their size. If the size of the dust is larger than the peak wavelength of the emission from the dust, its effective emissivity becomes high. Therefore the thermally balanced temperature of the larger dust is lower than the smaller dust. We calculate the equilibrium temperature of the larger sized dust with "DUSTY". The result for Mz3 case is displayed in Figure 5.4. Dust temperature in torus and equatorial

torus size of Mz3 derived from our observations are 90 K and > 4,300 AU respectively. This suggests that larger dust with a radius of > 1.0 μm is needed to explain our observations.

So far some observational evidences of the grain growth have been reported by previous studies. Jura et al. (1995) suggested that the dust in the disk around the post AGB star Red Rectangle may grow up to 20 μm. In other post-AGB star studies, mm-size dust grain growth in the disks or tori is indicated by Sahai et al. (2011), and de Ruyter et al. (2006). However, all of the grain growth mentioned here occurs in long-lived disks around the star evolved from the low mass progenitors. If the tori observed here are expanding as discussed in the previous section, the situation is completely different from these previous studies.

Since the growth rate of the dust should be proportional to square of the density of seed molecules, it would be possible to grow up the dust grains rapidly if the torus is dense enough. Peretto et al. (2007) pointed out the gas velocity at the equatorial plane in NGC6302 is 8 km/s. This value is almost similar to typical speed of AGB wind ~10 km/s. We employ the value of 10 km/s as a gas velocity at equatorial plane. Our observations have shown that the torus size in the equatorial direction of NGC6302, Mz3, and Hb5 are less than 4,100, 4,300, 3,000 AU respectively. Therefore the life time of the tori is estimated to be less than 2,000 years. This is consistent to the transition time from the AGB to the PNe phase from 10^2 – 10^4 years (e.g. Sabbadin 1986; Dopita et al. 1987; Vassiliadis & Wood 1994). Thus the dust mass loss rate is typically 10^{-6} – 10^{-5} M$_\odot$/year. This corresponds to the total mass loss rate of 10^{-4} – 10^{-3} M$_\odot$/year if the gas to dust mass ratio is assumed to be 0.01. This is two or three order higher than the typical mass loss rate of Mira variables, and almost one order higher than that of OH/IR stars. This suggests that the gas density at the dust forming regions of the torus is also expected to be one to three order higher. It is noteworthy that the gas density may be additionally one order higher because the mass loss of the bipolar PNe concentrates on the equational direction. Such high mass loss rates may cause the effective grain growth at the dust forming region.

Grain growth in the circumstellar environment is a very important process to understand the evolution of the dust grains. However the details have remained unclear yet. Further investigations about the grain growth are definitely needed, and observations at the longer mid-infrared wavelengths should provide the key to understand it. In Figure 5.5, schematic drawing of the structure of bipolar planetary nebulae discussed in this section is shown.
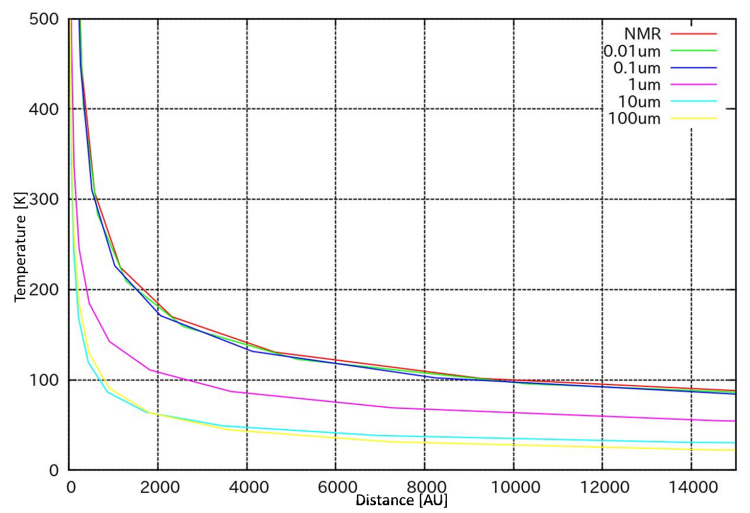
Figure 5.4: The calculation of thermal equilibrium temperatrue with different grain size in Mz3. NMR is standard dust size model.
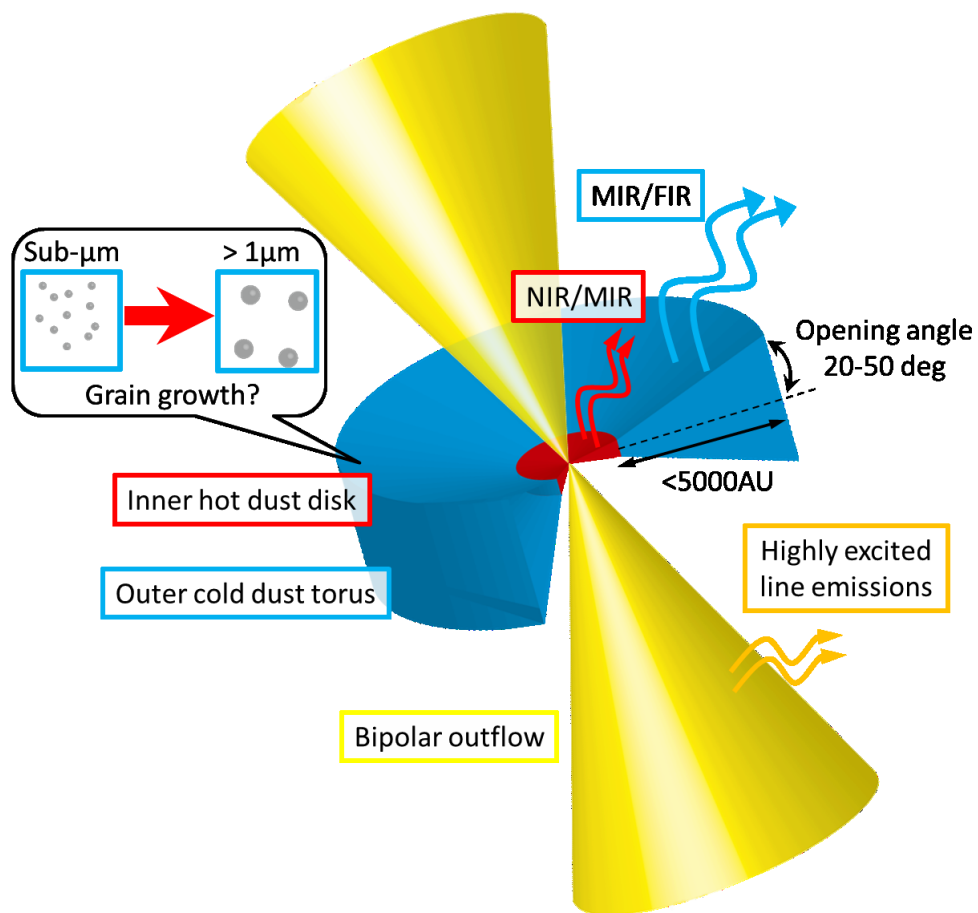
Figure 5.5: A schematic drawing of the structure of bipolar planetary nebulae.

Summary

In this paper we have carried out observations of three bipolar planetary nebulae, NGC6302, Mz3, Hb5. We successfully obtained mid-infrared images with high spatial resolution.

These are the first spatially resolved images of the planetary nebulae at the wavelengths longer than $30\,\mu$m. It is a surprising result that the unexpected bright $30\,\mu$m source was detected at the center of the nebulae. It suggests cold dust component exists close to the central star.

The mass of the cold dust component is estimated with the simple model. The estimated dust masses of NGC6302, Mz3, and Hb5 are 2.5×10^{-2}, 2.2×10^{-3}, and $1.0 \times 10^{-3} M_{\odot}$ respectively. These are up to 100 times larger than the dust mass estimated in previous studies. The morphological structure of the cold dust component has been estimated based on the ratio of the luminosity of the central star to the cold dust. It suggests that there are geometrical thick tori with opening angle of 50, 20, and 26 degree for NGC6302, Mz3, and Hb5.

In addition, the tori seem to be very compact even in the $30\,\mu$m images. This may be interpreted with two possibilities. One is the optical thickness. In this case, inner warm region which mainly absorbs the stellar radiation should be completely obscured by the outer cold torus, because the observations show there are no warm components in the spectral energy distribution. This requires that the outer torus is optically thick even at the shorter side of mid-infrared wavelengths. Furthermore the inner region needs to have almost the same opening angle as the outer torus.

The other possibility is dust grain growth in the torus. Since larger dust grains have relatively low emissivity, the thermally balanced temperature is lower than the smaller dust if they receive the same input radiation.

These results give the constraints on the structure of the dusty torus and provide important information to understand the strong mass loss on the equatorial plane.

Acknowledgments

References

Acker, A., Marcout, J., Ochsenbein, F., Stenholm, B., Tylenda, R., & Schohn, C. 1992, The Strasbourg-ESO Catalogue of Galactic Planetary Nebulae. Parts I, II.

Asano, K., Miyata, T., Sako, S., Kamizuka, T., Nakamura, T., Uchiyama, M., Yoneda, M., Kataza, H., Yoshii, Y., Doi, M., Kohno, K., Kawara, K., Tanaka, M., Motohara, K., Tanabe, T., Minezaki, T., Morokuma, T., Tamura, Y., Aoki, T., Soyano, T., Tarusawa, K., Kato, N., Konishi, M., Koshida, S., Takahashi, H., Handa, T., & Tateuchi, K. 2012, in Society of Photo-Optical Instrumentation Engineers (SPIE) Conference Series, Vol. 8446, Society of Photo-Optical Instrumentation Engineers (SPIE) Conference Series, 34

Bagnulo, S., Landstreet, J. D., Fossati, L., & Kochukhov, O. 2012, A&A, 538, A129

Balick, B. 1987, AJ, 94, 671

Blackman, E. G., Frank, A., Markiel, J. A., Thomas, J. H., & Van Horn, H. M. 2001, Nature, 409, 485

Bujarrabal, V., Castro-Carrizo, A., Alcolea, J., Van Winckel, H., Sánchez Contreras, C., Santander-García, M., Neri, R., & Lucas, R. 2013, A&A, 557, L11

Calvet, N., & Peimbert, M. 1983, Rev.Mexicana Astron, 5, 319

Castro-Carrizo, A., Neri, R., Bujarrabal, V., Chesneau, O., Cox, P., & Bachiller, R. 2012, A&A, 545, A1

Chesneau, O., Lykou, F., Balick, B., Lagadec, E., Matsuura, M., Smith, N., Spang, A., Wolf, S., & Zijlstra, A. A. 2007, A&A, 473, L29

Chevalier, R. A., & Luo, D. 1994, ApJ, 421, 225

Cohen, M., Kunkel, W., Lasker, B. M., Osmer, P. S., & Fitzgerald, M. P. 1978, ApJ, 221, 151

Cohen, M., Walker, R. G., Carter, B., Hammersley, P., Kidger, M., & Noguchi, K. 1999, AJ, 117, 1864

Corradi, R. L. M., & Schwarz, H. E. 1995, A&A, 293, 871

Cox, N. L. J., Kerschbaum, F., van Marle, A.-J., Decin, L., Ladjal, D., Mayer, A., Groenewegen, M. A. T., van Eck, S., Royer, P., Ottensamer, R., Ueta, T., Jorissen, A., Mecina, M., Meliani, Z., Luntzer, A., Blommaert, J. A. D. L., Posch, T., Vandenbussche, B., & Waelkens, C. 2012, A&A, 537, A35

de Ruyter, S., van Winckel, H., Maas, T., Lloyd Evans, T., Waters, L. B. F. M., & Dejonghe, H. 2006, A&A, 448, 641

Dopita, M. A., Meatheringham, S. J., Wood, P. R., Webster, B. L., Morgan, D. H., & Ford, H. C. 1987, ApJ, 315, L107

Draine, B. T., & Lee, H. M. 1984, ApJ, 285, 89

Frank, A. 1994, AJ, 107, 261

Gilman, R. C. 1974, ApJS, 28, 397

Greenhill, L. J., Moran, J. M., Backer, D. C., Bester, M., & Danchi, W. C. 1994, in Society of Photo-Optical Instrumentation Engineers (SPIE) Conference Series, Vol. 2200, Amplitude and Intensity Spatial Interferometry II, ed. J. B. Breckinridge, 304–315

Harvey, P. M., Bechis, K. P., Wilson, W. J., & Ball, J. A. 1974, ApJS, 27, 331

Icke, V. 1988, A&A, 202, 177

Indebetouw, R., Matsuura, M., Dwek, E., Zanardo, G., Barlow, M. J., Baes, M., Bouchet, P., Burrows, D. N., Chevalier, R., Clayton, G. C., Fransson, C., Gaensler, B., Kirshner, R., Lakićević, M., Long, K. S., Lundqvist, P., Martí-Vidal, I., Marcaide, J., McCray, R., Meixner, M., Ng, C.-Y., Park, S., Sonneborn, G., Staveley-Smith, L., Vlahakis, C., & van Loon, J. 2014, ApJ, 782, L2

Ivezic, Z., Nenkova, M., & Elitzur, M. 1999, ArXiv Astrophysics e-prints

Izumiura, H., Ueta, T., Yamamura, I., Matsunaga, N., Ita, Y., Matsuura, M., Nakada, Y., Fukushi, H., Mito, H., Tanabé, T., & Hashimoto, O. 2011, A&A, 528, A29

Jordan, S., Bagnulo, S., Werner, K., & O'Toole, S. J. 2012, A&A, 542, A64

Jordan, S., Werner, K., & O'Toole, S. J. 2005, A&A, 432, 273

Jura, M., Balm, S. P., & Kahane, C. 1995, ApJ, 453, 721

Kahn, F. D., & West, K. A. 1985, MNRAS, 212, 837

Kemper, F., Molster, F. J., Jäger, C., & Waters, L. B. F. M. 2002, A&A, 394, 679

Kwok, S., Purton, C. R., & Fitzgerald, P. M. 1978, ApJ, 219, L125

Le Bertre, T. 1992, A&AS, 94, 377

—. 1993, A&AS, 97, 729

Leone, F., Corradi, R. L. M., Martínez González, M. J., Asensio Ramos, A., & Manso Sainz, R. 2014, A&A, 563, A43

Leone, F., Martínez González, M. J., Corradi, R. L. M., Privitera, G., & Manso Sainz, R. 2011, ApJ, 731, L33

Little-Marenin, I. R., Stencel, R. E., & Staley, S. B. 1996, ApJ, 467, 806

Lockwood, G. W., & Wing, R. F. 1971, ApJ, 169, 63

López, J. A., García-Díaz, M. T., Steffen, W., Riesgo, H., & Richer, M. G. 2012, ApJ, 750, 131

Lord, S. D. 1992, A new software tool for computing Earth's atmospheric transmission of near- and far-infrared radiation, Tech. rep.

Maercker, M., Mohamed, S., Vlemmings, W. H. T., Ramstedt, S., Groenewegen, M. A. T., Humphreys, E., Kerschbaum, F., Lindqvist, M., Olofsson, H., Paladini, C., Wittkowski, M., de Gregorio-Monsalvo, I., & Nyman, L.-A. 2012, Nature, 490, 232

Manchado, A., Villaver, E., Stanghellini, L., & Guerrero, M. A. 2000, in Astronomical Society of the Pacific Conference Series, Vol. 199, Asymmetrical Planetary Nebulae II: From Origins to Microstructures, ed. J. H. Kastner, N. Soker, & S. Rappaport, 17

Matsuura, M., Dwek, E., Meixner, M., Otsuka, M., Babler, B., Barlow, M. J., Roman-Duval, J., Engelbracht, C., Sandstrom, K., Lakićević, M., van Loon, J. T., Sonneborn, G., Clayton, G. C., Long, K. S., Lundqvist, P., Nozawa, T., Gordon, K. D., Hony, S., Panuzzo, P., Okumura, K., Misselt, K. A., Montiel, E., & Sauvage, M. 2011, Science, 333, 1258

Matsuura, M., Zijlstra, A. A., Molster, F. J., Waters, L. B. F. M., Nomura, H., Sahai, R., & Hoare, M. G. 2005, MNRAS, 359, 383

Mauron, N., & Huggins, P. J. 1999, A&A, 349, 203

Miyata, T., Sako, S., Kamizuka, T., Nakamura, T., Asano, K., Uchiyama, M., Konishi, M., Yoneda, M., Takato, N., Yoshii, Y., Doi, M., Kohno, K., Kawara, K., Tanaka, M., Motohara, K., Minezaki, T., Tanabe, T., Morokuma, T., Tamura, Y., Aoki, T., Soyano, T., Tarusawa, K., Takahashi, H., Koshida, S., & Kato, N. M. 2012, in Society of Photo-Optical Instrumentation Engineers (SPIE) Conference Series, Vol. 8444, Society of Photo-Optical Instrumentation Engineers (SPIE) Conference Series, 6

Miyata, T., Sako, S., Nakamura, T., Onaka, T., & Kataza, H. 2008, in Society of Photo-Optical Instrumentation Engineers (SPIE) Conference Series, Vol. 7014, Society of Photo-Optical Instrumentation Engineers (SPIE) Conference Series, 28

Monnier, J. D., Geballe, T. R., & Danchi, W. C. 1998, ApJ, 502, 833

Morris, M. 1981, ApJ, 249, 572

Peeters, E., Hony, S., Van Kerckhoven, C., Tielens, A. G. G. M., Allamandola, L. J., Hudgins, D. M., & Bauschlicher, C. W. 2002, A&A, 390, 1089

Peretto, N., Fuller, G., Zijlstra, A., & Patel, N. 2007, A&A, 473, 207

Persi, P., Cesarsky, D., Marenzi, A. R., Preite-Martinez, A., Rouan, D., & Siebenmorgen, R. 1999, in ESA Special Publication, Vol. 427, The Universe as Seen by ISO, ed. P. Cox & M. Kessler, 389

Pottasch, S. R., & Surendiranath, R. 2007, A&A, 462, 179

Quinn, D. E., Moore, T. J. T., Smith, R. G., Smith, C. H., & Fujiyoshi, T. 1996, MNRAS, 283, 1379

Ramos-Larios, G., Guerrero, M. A., Suárez, O., Miranda, L. F., & Gómez, J. F. 2009, A&A, 501, 1207

—. 2012, A&A, 545, A20

Rice, M., Schwarz, H., & Monteiro, H. 2004, in Bulletin of the American Astronomical Society, Vol. 36, American Astronomical Society Meeting Abstracts, 138.13

Robertson-Tessi, M., & Garnett, D. R. 2005, VizieR Online Data Catalog, 215, 70371

Sabbadin, F. 1986, A&AS, 64, 579

Sahai, R., Claussen, M. J., Schnee, S., Morris, M. R., & Sánchez Contreras, C. 2011, ApJ, 739, L3

Sako, S., Aoki, T., Doi, M., Handa, T., Kawara, K., Kohno, K., Minezaki, T., Mitani, N., Miyata, T., Motohara, K., Soyano, T., Tanabe, T., Tanaka, M., Tarusawa, K., Yoshii, Y., Bronfman, L., & Ruiz, M. T. 2008, in Society of Photo-Optical Instrumentation Engineers (SPIE) Conference Series, Vol. 7012, Society of Photo-Optical Instrumentation Engineers (SPIE) Conference Series, 2

Schaeidt, S. G., Morris, P. W., Salama, A., Vandenbussche, B., Beintema, D. A., Boxhoorn, D. R., Feuchtgruber, H., Heras, A. M., Lahuis, F., Leech, K., Roelfsema, P. R., Valentijn, E. A., Bauer, O. H., van der Bliek, N. S., Cohen, M., de Graauw, T., Haser, L. N., van der Hucht, K. A., Huygen, E., Katterloher, R. O., Kessler, M. F., Koornneef, J., Luinge, W., Lutz, D., Planck, M., Spoon, H., Waelkens, C., Waters, L. B. F. M., Wieprecht, E., Wildeman, K. J., Young, E., & Zaal, P. 1996, A&A, 315, L55

Sloan, G. C., Kraemer, K. E., & Price, S. D. 2003, in ESA Special Publication, Vol. 481, The Calibration Legacy of the ISO Mission, ed. L. Metcalfe, A. Salama, S. B. Peschke, & M. F. Kessler, 447

Smith, B. J., Leisawitz, D., Castelaz, M. W., & Luttermoser, D. 2002, AJ, 123, 948

Smith, N. 2003, MNRAS, 342, 383

Smith, N., & Gehrz, R. D. 2005, AJ, 129, 969

Soker, N. 1998, ApJ, 496, 833

Soker, N., & Rappaport, S. 2000, ApJ, 538, 241

Stanghellini, L., Villaver, E., Manchado, A., & Guerrero, M. A. 2002, ApJ, 576, 285

Szyszka, C., Walsh, J. R., Zijlstra, A. A., & Tsamis, Y. G. 2009, ApJ, 707, L32

Tocknell, J., De Marco, O., & Wardle, M. 2014, MNRAS, 439, 2014

Vassiliadis, E., & Wood, P. R. 1994, ApJS, 92, 125

Yoshii, Y., Doi, M., Handa, T., Kawara, K., Kohno, K., Minezaki, T., Mitsuda, K., Miyata, T., Motohara, K., & Tanaka, M. 2002, in 8th Asian-Pacific Regional Meeting, Volume II, ed. S. Ikeuchi, J. Hearnshaw, & T. Hanawa, 35–36

Yoshii, Y., Doi, M., Kohno, K., Miyata, T., Motohara, K., Kawara, K., Tanaka, M., Minezaki, T., Sako, S., Morokuma, T., Tamura, Y., Tanabe, T., Takahashi, H., Konishi, M., Kamizuka, T., Koshida, S., Kato, N., Aoki, T., Soyano, T., Tarusawa, K., Handa, T., Bronfman, L., Ruiz, M. T., Hamuy, M., & Mendez, R. 2014, in Society of Photo-Optical Instrumentation Engineers (SPIE) Conference Series, Vol. 9145, Society of Photo-Optical Instrumentation Engineers (SPIE) Conference Series, 7